Enhancement of friction factors for microchannels fabricated using laser powder directed energy deposition

Gradl, P.R.; Cervone, A.; Colonna, Piero

DOI
10.1016/j.matdes.2025.113673

Publication date
2025

Document Version
Final published version

Published in
Materials & Design

Citation (APA)
Gradl, P. R., Cervone, A., & Colonna, P. (2025). Enhancement of friction factors for microchannels fabricated using laser powder directed energy deposition. *Materials & Design*, *251*, Article 113673. https://doi.org/10.1016/j.matdes.2025.113673

Materials & Design 251 (2025) 113673

Contents lists available at ScienceDirect

Materials & Design

journal homepage: www.elsevier.com/locate/matdes

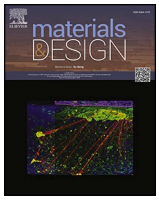

Enhancement of friction factors for microchannels fabricated using laser powder directed energy deposition

Paul Gradl [a,*], Angelo Cervone [b], Piero Colonna [c]

[a] Propulsion Department, NASA Marshall Space Flight Center, Huntsville, AL, United States
[b] Space Systems Engineering, Delft University of Technology, Delft, Netherlands
[c] Propulsion and Power, Delft University of Technology, Delft, Netherlands

ARTICLE INFO

Keywords:
Additive Manufacturing
Directed Energy Deposition
Microchannels
Surface Enhancements
Polishing
Friction Factor
Hydraulic Diameter

ABSTRACT

Designing high-performance and aerospace-grade heat exchangers requires detailed characterization of the as-manufactured geometry, including cross-sectional area and surface texture, to reduce uncertainties in performance prediction and issues regarding subsequent system integration. This paper presents experimental testing and analysis of microchannels fabricated using the laser powder directed energy deposition (LP-DED) additive manufacturing (AM) process. Research has shown that as-built surfaces result in differential pressure higher than what is predicted with current correlations and surface enhancements may be required for heat exchangers built using AM to meet the desired pressure drop specifications. Various surface enhancement techniques including abrasive flow machining (AFM), chemical milling (CM), and chemical mechanical polishing (CMP), were applied to the internal surfaces of the channels to tailor flow dynamics and induce variations in pressure drop. Based on experimental flow testing, channels processed with surface enhancements provide a tenfold reduction in differential pressure compared to the as-built channels. After testing, the samples were destructively sectioned to obtain geometric and detailed surface texture information. This characterization helped to inform a new prediction method for determining hydraulic diameter and equivalent sand grain roughness, thus reducing the uncertainty of predicted friction factors. The new correlation allows to estimate friction factor and pressure drop with a deviation from the experimental data that is within 20% of their value. The identification of the mechanisms at the basis of the formation of surface texture allowed to categorize distinct aspects related to friction factor ranges: roughness peaks, peak smoothing/reduction, minimized roughness, and combined waviness and valley reduction.

1. Introduction

Critical design features of high-performance, aerospace-grade heat exchangers include the geometry of internal channels and their surface finish. These characteristics are fundamental for the transfer of thermal energy between fluids and the flow friction, which ultimately determine whether the component and the overall system function properly. Designing these channels is often an iterative process that aims to minimize the associated pressure loss, maximize heat transfer, and maximize the service life of the component. Optimizing pressure drop, heat transfer, and fatigue life involves compromising between contrasting requirements. Surface texture significantly affects pressure losses and heat transfer. Prior research characterized the geometry of thin-wall laser powder directed energy deposition (LP-DED) microchannels [1–3] and the related first-order flow resistance in terms of discharge coefficient [4]. This current research focuses on the study of friction factors, their relationship with sand grain roughness and the derivation of a correlation, the definition of hydraulic diameter suitable for this case, and the correlations for the prediction of pressure losses in square microchannels.

The Moody diagram, established decades ago, provides nondimensional values of the friction factor as a function of the Reynolds number and relative pipe roughness [5]. Moody developed this diagram, valid for laminar and turbulent flows, using experimental data from Darcy-Weisbach and Nikuradse [6,7]. Relative pipe roughness relates the height of surface roughness to the hydraulic diameter, however it cannot provide a merit parameter that is adequate for the complexity of additively manufactured (AM) surfaces and its relationship to the original sand grain roughness characterizing the experimental data of

* Corresponding author.
E-mail address: paul.r.gradl@nasa.gov (P. Gradl).

https://doi.org/10.1016/j.matdes.2025.113673
Received 11 November 2024; Received in revised form 7 January 2025; Accepted 24 January 2025
Available online 25 January 2025

Nomenclature

A	area (mm^2)
A_{AB}	Average area of as-built channels
A_{Ch}	Area of channel being measured
AB	As-built
AFM	Abrasive flow machining
AM	Additive Manufacturing
BD	Build direction
Cd	Discharge coefficient
CM	Chemical milling
CMP	Chemical mechanical polishing
CV	Coefficient of variation
ΔP	differential pressure (bar)
DED	directed energy deposition
DfAM	Design for additive manufacturing
D_h	Hydraulic diameter
D_{h1}	Hydraulic diameter, based on $\sqrt{A_{meas}}$
D_{h2}	Adjusted hydraulic diameter for texture
f_A	Friction Factor, Avci and Kargoz
f_B	Friction Factor, Brkic and Cojbasic
f_C	Friction Factor, Colebrook-White
f_D	Friction Factor, Darcy
f_M	Friction Factor, based on Moody
f_s	Friction Factor, Swamee and Jain
f_T	*Friction Factor,* Mileikovskyi and Tkachenko
g_c	gravitational constant
K_s	Sand grain roughness
λc	large-scale band pass filter (also Lc)
λs	small-scale (noise) filter (also Ls)
LP-DED	Laser Powder Directed Energy Deposition
$\dot{m}$	mass flow rate (kg/sec)
MR	material removal (um)
NASA HR-1	Fe-Ni-Cr Hydrogen Resistant superalloy
P	perimeter (mm)
[P]	Primary filtering (waviness and roughness)
Pa	Directional 2D profile average height
Pp	2D Profile Peak Height
PSD	Particle Size Distribution
Psk	2D Profile Skewness
PT	pressure transducer
Pv	2D Profile Valley depth
Pz	Average Maximum Profile Height
[R]	Roughness filtered
Re	Reynolds number
ρ	density of water ($grams/cm^3$)
Ra	Arithmetic mean directional roughness (λc at 0.8 mm)
Rk	2D directional core roughness (λc at 0.8 mm)
Rz	Average directional maximum profile height (λc at 0.8 mm)
S_T	measured surface texture/roughness
Sa	Average areal texture
SEM	Scanning Electron Microscope
Sk	Core texture depth
Sp	Maximum peak height
Spd	Roughness Peak Density
Spk	reduced peak height
Sq	Root mean square (RMS) height
Sv	Maximum valley depth
Svk	Reduced valley depth
Sz	Maximum surface height
TC	thermocouple
u	dynamic viscosity (Pa-s)
v	kinematic viscosity (m^2/sec)
Vvv	dale void volume ($\mu m^3/\mu m^2$)
W	Watts
Wa	Arithmetic mean directional waviness (λc at 0.8 mm)
Wp	Waviness peak height (λc at 0.8 mm)
WPc	Waviness peak density (λc at 0.8 mm)

Darcy–Weisbach and Nikuradse. The proportionality relationship between relative roughness and friction factor is well known: as roughness increases, the friction factor also increases, and this is mathematically expressed by the Colebrook-White correlation [8,9].

Early experiments by Darcy, Nikuradse, and Colebrook were limited to values of relative roughness lower than 5 % [10]. Researchers like Kandlikar et al. expanded the measurement range to values of relative roughness up to 14 % [11]. AM offers several advantages if adopted for the fabrication of special heat exchangers, especially in terms of complexity and miniaturization of channels, therefore it is becoming more prominent. However, traditional correlations for the modeling of the fluid dynamic effect of surface texture perform very poorly in case of surfaces obtained with AM, resulting in actual values of the friction factor that are higher than those predicted by correlations based on prior experimental data [12]. McClain et al. [13] highlighted the necessity of accurately characterizing and measuring surface texture and equivalent sand grain roughness for accurate predictions because the roughness to hydraulic diameter ratio is high, and outside the range of validity of current correlations.

Several authors have investigated flow friction associated with simple- and complex-geometry channels made with L-PBF and as-built surfaces. Richermoz et al. [14] experimented on circular and round channels made of Alloy 600 and manufactured with laser powder bed fusion (L-PBF). The channels featured alternating 90° serpentine bends. They measured a 37 % increase in friction factor over traditionally manufactured channels. However, they noted that uncertainty in hydraulic diameter affected the results, which were measured using computed tomography (CT) and basic directional roughness measurements. Zhou et al. [15] investigated changes of hydraulic diameter in L-PBF-made channels, depending on build angle, dross formation, and warping. They proposed a linear model adjustment but did not relate such adjustment to physical geometry. These differences highlight the importance of perimeter biasing due to internal channel texture as this affects the hydraulic diameter.

Snyder et al. [16] reported that varying L-PBF parameters reduced surface roughness by 50 %, resulting in a proportional reduction of the friction factor. Kirsch et al. [17] found a three-fold increase in friction factor with a 30 % difference in hydraulic diameter at Reynolds numbers from 3,000 to 10,000. Hartsfield et al. [18] concluded that sand grain roughness does not correlate with profilometer roughness measurements of L-PBF surfaces. These researchers therefore proposed to approximate the value of sand grain roughness as 50 % of the mean powder diameter. Zhu et al. [19] estimated that values of relative roughness can be estimated by multiplying the average areal surface texture (Sa) from each surface by a factor of two. This work considered solely L-PBF-made horizontal round tubes with diameters greater than 6 mm and as-built surfaces. Jamshidinia et al. [20] put into evidence that surface roughness resulting from L-PBF is related to process heat input, emphasizing the importance of build parameters. However, the friction factor correlations they obtained cannot be broadly applied to channels produced with different AM processes.

Most documented research on flow friction associated with AM channels focused on channels with as-built surfaces, thus no post-processing of the surfaces was considered. Favero et al. [21]

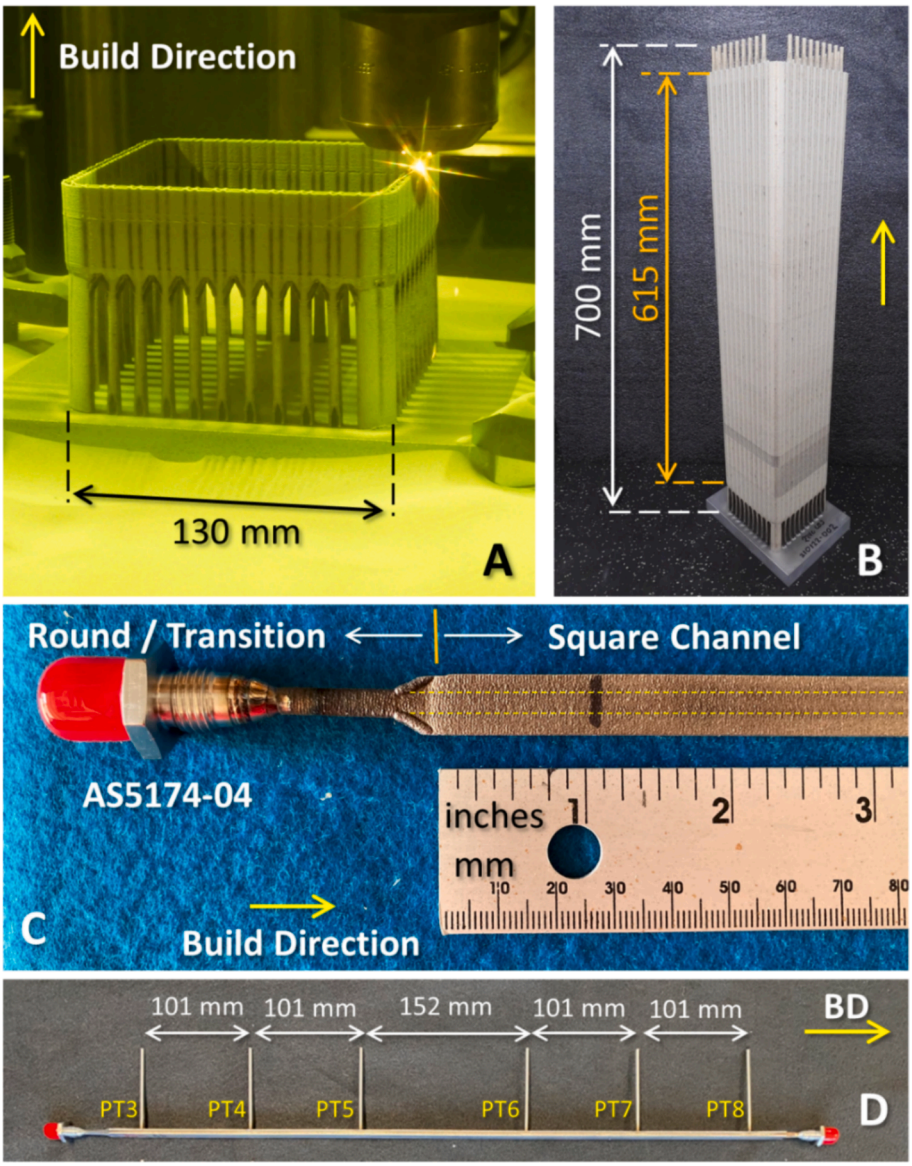

Fig. 1. Channel sample fabrication. A) LP-DED build of boxes with multiple channels, B) Completed boxes following deposition, C) Laser-welded fittings; the square channel width is indicated by yellow dotted lines, D) Channel with welded inlet and outlet fittings and distances between ports. (For interpretation of the references to color in this figure legend, the reader is referred to the web version of this article.)

performed friction measurements on oval copper channels made with L-PBF and post–processed with chemical milling. They concluded that pressure drop could be reduced by an order of magnitude with a six-fold reduction in average roughness. The developed correlations are based on a hydraulic diameter calculated using area and perimeter, but no sand grain roughness was considered. Vijetha et al authored a review article that mentions the importance of hydraulic diameter and surface texture for microchannels using AM, but also describe the definition of hydraulic diameter using perimeter and area [22]. Kaur and Singh [23] emphasized the need for thorough research on the localized influence of surface texture.

The build mechanics of the LP-DED is fundamentally different from that of L-PBF. Results regarding the flow friction of channels made with L–PBF cannot be applied broadly and friction factors associated to channels made with LP-DED are expected to vary due to differences in powder feedstock, process parameters, and environmental process factors like purges and surrounding powder. The derivation of friction factor correlations is further complicated if surfaces are enhanced with different post-processing methods.

Comprehensive experimental data and correlations valid for AM microchannels with similar geometry and different surface texture are not available yet. Full characterization of surface topography is crucial to understand the underlying mechanisms causing the texture. Moreover, such surface enhancement methods enable the possibility to improve the internal channel finish and reduce flow resistances through post-processing. The study aimed to characterize surface enhancement post-processing methods and their influence on flow resistance, prioritizing evaluation over optimization for a “smooth” surface. Designers of additively manufactured heat exchangers require options to prescribe surface finishing to tune the flow characteristics to meet design objectives, rather than accepting as the only option what results from as-built surfaces. This approach leverages AM to balance heat transfer, fluid friction, corrosion resistance, mechanical fatigue life, and aesthetics. This research summarizes therefore an experimental study to determine the pressure drop associated with square channels fabricated with LP–DED and processed with various surface enhancements, resulting in a wide range of surface textures and topographies. The experimental data allowed to establish 1) a new definition of hydraulic diameter

Table 1
Chemical composition of the NASA HR-1 powder utilized to build the channel samples (HMI Lot HRA11/Coarse and HRA9/Fine).

Size		Fe	Ni	Cr	Co	Mo	Ti	Al	V	W
Coarse	Wt. %	Bal.	33.98	14.74	3.78	1.84	2.36	0.24	0.3	1.6
Fine	Wt. %	Bal.	33.91	14.66	3.79	1.83	2.41	0.24	0.3	1.6

which eliminates perimeter bias due to surface texture, 2) an equivalent sand grain roughness, and 3) new correlations that considerably improve friction factor predictions for such channels. The surface texture characteristics are evaluated in detail, providing roughness and waviness attributes which can be directly related to the friction factor.

2. Methodology

Channel samples were fabricated specifically for differential pressure drop testing. The experimental campaign took place at NASA Marshall Space Flight Center in a high-pressure water flow facility. The test sections of the square microchannels were approximately 615 mm in length. Numerous channels were fabricated and tested in their as-built condition, while several others underwent surface enhancements prior to testing using abrasive flow machining (AFM), chemical milling (CM), and chemical mechanical polishing (CMP) processes. After the testing phase, the channel samples were sectioned to characterize the internal surface and flow area to validate assumptions for the analysis and correlations.

2.1. Fabrication of DED samples and processing

The 615 mm length test channels were designed with a nominal width and height of 2.54 x 2.54 mm and built using LP-DED. They are shown in Fig. 1. The square test section included a length of 615 mm with a 25 mm blended transition segment from the square channel to a round extrusion on both ends (Fig. 1C). This design facilitated the welding of a universal AN-type fitting onto either end as an interface with the the facility. The channels were constructed on an RPMI 557 LP-DED machine with an argon-inert build chamber, utilizing an A36 mild steel base plate. The boxes were built using consistent parameters, including a laser power of 350 W, powder feed rate of 23 g/min, travel speed of 763 mm/min, and a layer height of 0.254 mm.

Coarse powder feedstock was rotary atomized by Homogenized Metals Inc. (HMI), featuring a particle size distribution (PSD) ranging from 45 to 105 μm and an average measured size of 73 μm. Notably, the oxygen content measured 68 ppm, and the nitrogen content was 12 ppm. The HMI fine powder featured a PSD of 10–45 μm and average size of 32 μm. The oxygen content was 145 ppm and nitrogen was 10 ppm. The higher oxygen content in the fine powder is attributed to the larger area per volume of the powder. The composition, as determined using ICP, is detailed in Table 1. Virgin powder was employed for all builds.

The channels were initially fabricated as larger boxes, as illustrated in Fig. 1, and then underwent stress relief (1066 °C for 90 min with a slow furnace cooling), homogenization (1163 °C for 6 h in vacuum and Argon-quenched), solution annealing (1066 °C for 60 min, with an Argon-quench), and double aging (690 °C for 16 h, cooled to 621 °C and held for 16 h; 32 total hours). Following the heat treatment, the boxes were removed from the build plate using a bandsaw. Subsequently, the boxes were individually sectioned using water jet cutting and the ends of the channels were machined in preparation for the welding of the ports. The channels were cleaned, and subsequently an AS5174-04 Inconel 625 fitting was laser-welded to each of the inlets and outlets of the samples (Fig. 1C). The channel that was tested is indicated by the yellow lines, and stock regions were fabricated to either side of the channel to allow it to be sectioned.

Following the surface enhancement of the internal perimeter, a 0.75 mm diameter hole was drilled at six locations for the pressure transducer port tubes (sequentially tagged as PT03 through PT08), and a 3.175 mm diameter tube was laser welded, as depicted in Fig. 1D. PT01 and PT02 were used for the measurement of the tank pressure prior to the test article. The distances between the tubes are shown in Fig. 1D, while some distances varied slightly for PT6-PT7.

In addition to the baseline as-built samples and those whose surfaces were enhanced, additional as-built samples were fabricated with a round channel and a larger area of the square channel. The intended use of the round channels was to provide an appropriate hydraulic diameter conversion from the round to square channels. The channels with larger area were conceived to investigate the comparison between channels with surfaces in the as-–built condition and channels with modified

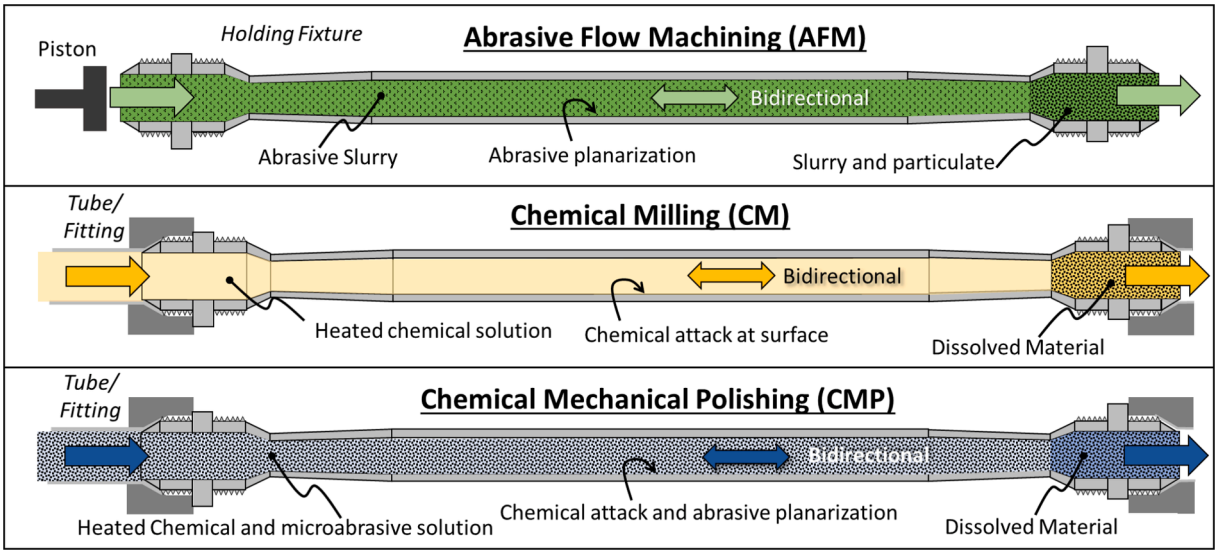

Fig. 2. Overview of Abrasive Flow Machining (AFM), Chemical Milling (CM), and Chemical Mechanical Polishing (CMP) used to process 615 mm length LP-DED microchannels. Channels and setup apparatus are not shown to scale. Illustration revised from [4].

Table 2
Characteristics and nomenclature of the tested channels.

Channel Identifier	Surface Enhancement Process	Notes	Target Channel Geometry (mm)
AB-xx	None	As-built surface; **Coarse 45–105 µm powder**	2.54 x 2.54 (width/height)
AFM-xx	Abrasive Flow Machining	Slurry extrusion pressure of 69 bar; flow rate ranging from 0.56 L/min to 4.47 L/min	2.54 x 2.54 (width/height)
CM-xx	Chemical Milling	Hydrofluoric acid; temperature 52 to 60 °C; and exposure from 4 to 19 mins	2.54 x 2.54 (width/height)
CMP-xx	Chemical Mechanical Polishing	Flow rate 0.4 to 2 L/min; temperature 50 to 60 °C; exposure from 10 to 20 mins; up to 10 % microabrasives	2.54 x 2.54 (width/height)
AB-53	None	As-built surface; **Fine 15–45 µm powder**	2.54 x 2.54 (width/height)
AB-54-L	None	As-built surface; **15–45 µm powder**	2.95 x 2.95 (width/height)

surfaces but with an equivalent cross-–sectional area. The round (tube) channels were designed with a diameter of 2.87 mm to match the cross-sectional area of the square channels, but shrank to a diameter of ~ 2.7 mm. The larger square channels were designed to be 2.95 mm in height and width.

2.2. Surface enhancements of microchannels

A range of surface conditions (i.e., variations) of the internal microchannels was obtained using abrasive flow machining (AFM), chemical milling (CM), and chemical mechanical polishing (CMP). These enhancement processes were chosen for their ability to modify the internal surface with cross-sections smaller than 2.54 x 2.54 mm [24–26]. The primary goal of this research was to analyze how varying the internal surface with the enhancement methods influence the fluid flow resistance, rather than minimizing roughness or achieving optimal polishing (i.e., full smoothing). An overview of the process setup for AFM, CM, and CMP is illustrated in Fig. 2.

AFM uses a viscous polymer slurry containing abrasive particles, pressurized and pumped through channels in single or bi-directional flow [27]. This action abrades the surface, and the removed material is carried away by the slurry. This method, also known as extrude-honing or slurry-honing, adjusts slurry type, volume, duration, and cycle count to tailor channel surfaces. The AFM samples in this study were flowed bidirectionally. CM involves flowing a chemical solution through the channels to dissolve the surface metal by attacking the grain structure [28,29]. The dissolved material is flushed out with the hydrofluoric solution, and longer exposure times result in greater material removal. Parts are rinsed and deactivated after chemical machining. CMP combines chemical and mechanical forces to reduce surface

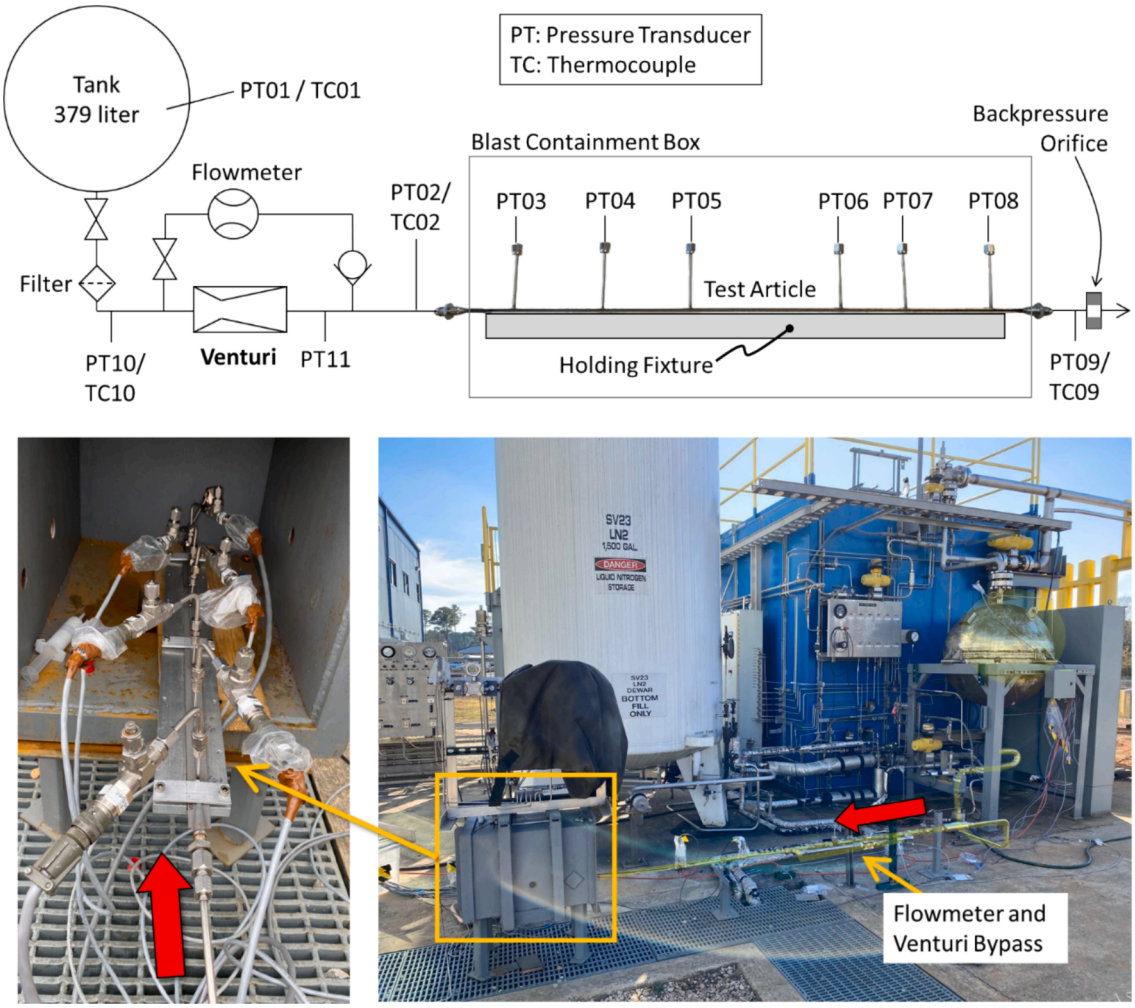

Fig. 3. Schematic and images of the experimental setup and test facility developed and used to test 615 mm length channels.

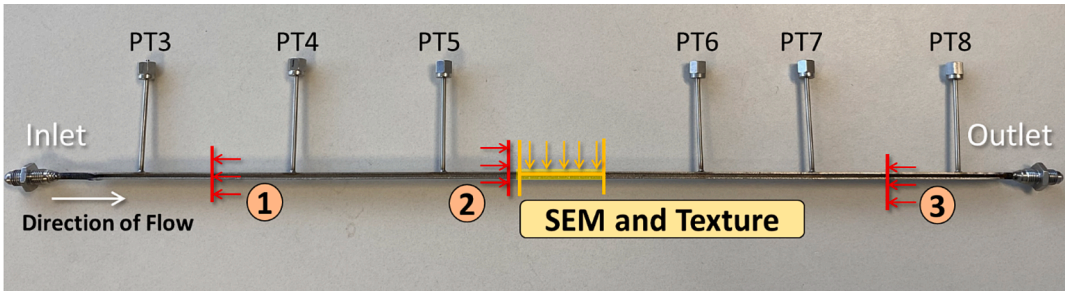

Fig. 4. Location of the sectioning of the 615 mm length channels. The direction of the flow is the same as the direction of the build.

roughness by selectively removing material [30]. The chemical solution removes most material, while abrasive media planarizes the surface. The process involves flowing a chemical solution with micro-abrasives through the channels, flushing removed particles with the solution. Variables such as solution flow rate, temperature, process duration, and abrasive weight were adjusted for each channel.

A detailed discussion of the surface enhancement methods used in the sample fabrication can be found in [4]. The channel configurations and the range of processing parameters for each sample are summarized in Table 2. The samples processed with the varying surface enhancements were built with coarse powder (45–105 μm). The samples are identified according to the process type along with a letter and/or number designation (i.e., AB-xx, AFM-xx, CM-xx, CMP-xx) and detailed in Supplemental.

2.3. Test Configuration and Procedures

The water flow facility available at NASA Marshall Space Flight Center was used for the experimental campaign aimed at obtaining friction factors. The schematic of the test setup is shown in Fig. 3. The 379-liter GN_2 pressurized tank was filled with deionized (DI) water and a 10 μm filter was incorporated downstream of the tank after the main valve. A Potter Aero RAA-1/2–301-1/2-5440A (±0.1 % full range) flowmeter (3.4 to 36 l/min) was installed in a bypass leg of the system in addition to a 1.016 mm diameter cavitating venturi (Cd = 0.980) to control the mass flow through the channel test articles. The venturi cross-sectional area was sized to be smaller than the smallest cross-section area of the test article. The Wika Tecsis 99–6776-0002 (0–138 bar) pressure transducers (PT), with an accuracy of ± 0.05 %, and Omega Type E thermocouples (TC) with an accuracy of ± 1.7 °C, were installed at locations indicated on the diagram of Fig. 3. The test article was installed in a blast containment due to the operating pressures. All instrumentation were all calibrated prior to installation and checks were completed each day of testing.

The test articles were bolted into a fixture within a groove to hold the channel sample to eliminate distortion that could be caused by water pressurization or residual stress. Each channel test article was flushed with deionized (DI) water at 7 bar for a minimum of 10 s prior to data collection. The tank was then pressurized at increments of 34, 69, 138 Bar and held for 10 s at each pressure with water flowing through both the flow meter and a cavitating venturi (1.106 mm dia. throat). The cavitation of the venturi was verified based on the exit to inlet pressure ratio (<0.80) for each test run. A second set of data was collected at identical tank pressures bypassing the venturi allowing for the flow rate to be maximized for each channel. A Dewetron data acquisition system was used in conjunction with the LabVIEW software for system control. Six sets of data were collected per channel sample.

After testing was completed, all recorded data were tabulated for each of tested channel and each tank pressure set point. At each pressure set point, the pressure was kept constant, and data acquired for approximately 10 s. The finite pressure differential is obtained by subtracting values of absolute pressures at the selected ports. Mass flow was measured using the flow meter.

The necessary fluid properties were obtained for each data set and run. The density of water (g/cc) was calculated with a reference model [31] using the average temperature at the inlet and outlet of the channel and the average channel pressure to identify the thermodynamic state. The dynamic viscosity (Pa-s) at the same thermodynamic state was obtained as

$$\mu = \mathrm{v}\rho \tag{1}$$

where v is the kinematic viscosity (m^2/sec) and ρ is the fluid density.

The mass flow rate is defined as

$$\dot{m} = \rho A v, \tag{2}$$

where ρ is the fluid density, A is the area, and v is the linear velocity. The fluid velocity can therefore be obtained as

$$v = \frac{\dot{m}}{\rho A}, \tag{3}$$

with measured values for $\dot{m}$ and A.

2.4. Post-test channel measurements

2.4.1. Port distance measurements

After the testing was complete, the channels were visually inspected and measured using Mitutoyo 500–160-30 (±0.02 mm) and Mitutoyo 500–506-10 (±0.05 mm) calipers to obtain the as-produced geometry. The procedure to obtain the center of the tube port was to measure between each port on the outside of the instrumentation tubes and subtract the value of the diameter of the tube. The nomenclature of full, mid, and short distances was representative of the distances between pressure transducers PT3-PT8, PT4-PT8, and PT5-PT6, respectively. The maximum error determined between these measurements was determined to be 0.043 % for the full length and 0.1 % for the mid length.

2.4.2. Sectioning of the channels

Following visual inspections and port distance measurements, the channel samples were sectioned to determine their cross-sectional area, perimeter, surface texture, and microstructure details. Three sections, perpendicular to the flow, were taken (Fig. 4): the first at the midpoint between PT3 and PT4, the second offset from the center between PT5 and PT6, and the third at the midpoint between PT7 and PT8. These sections, selected along the length of the channel, allow to evaluate any axial length variations resulting from surface enhancement processing. The samples were tagged according to the channel number, with −1, −2, and −3 suffixes for traceability during microscopic imaging. Destructive evaluation of the samples was selected over X-ray computer tomography (XCT) based on the required resolution for directly measuring surface texture parameters, cross-sectional area, and flow perimeter [4,32,33].

2.4.3. Optical Images, SEM, and surface texture characterization

The samples from the sections (−1, −2, and −3) were mounted,

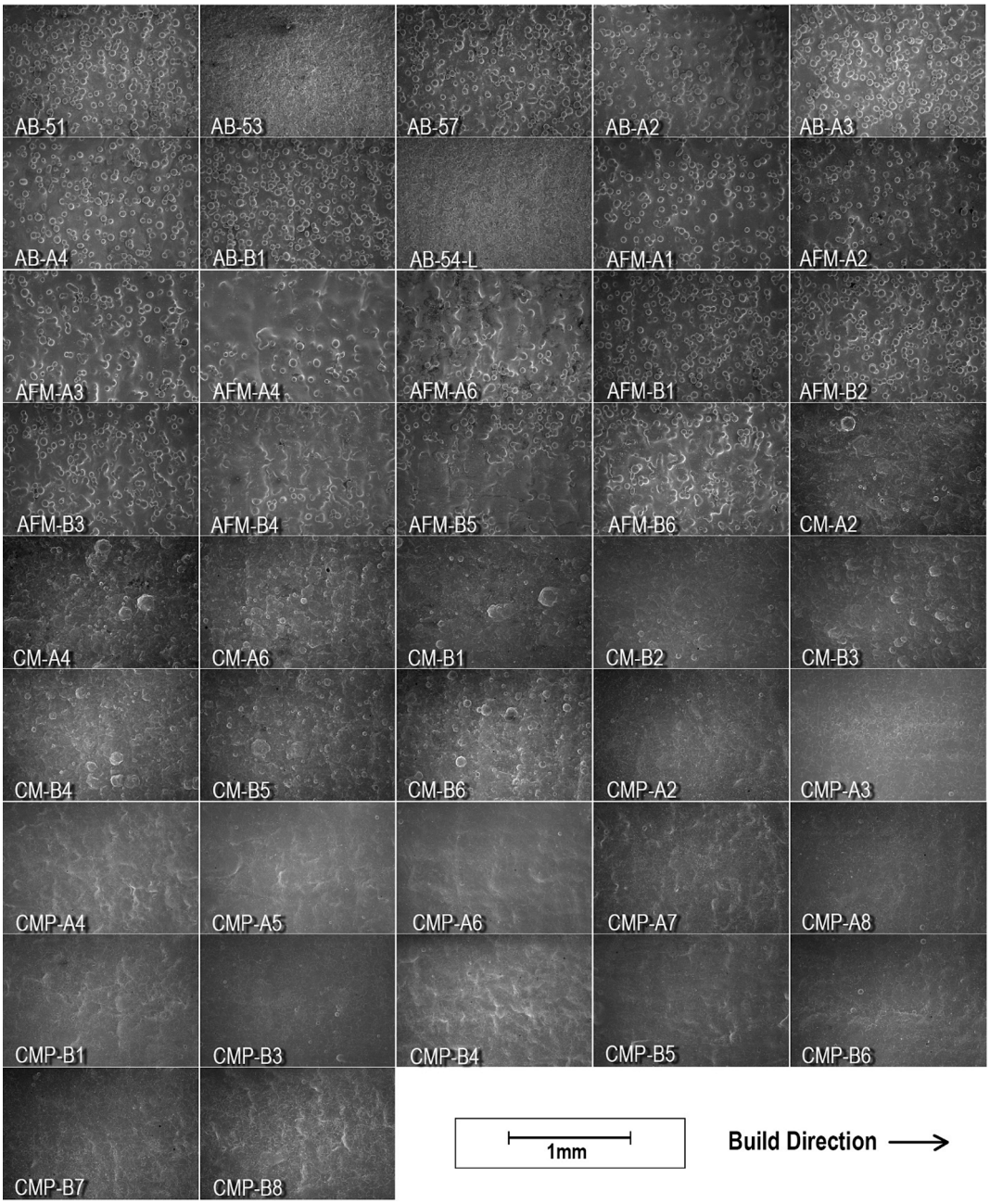

Fig. 5. SEM images of the inner surfaces of the 615 mm length square channel samples.

polished, and etched. All optical images were obtained using a Keyence VHX digital microscope. The images were processed using the software *Image J* (Version 1.53e) [34]. The values obtained for the area and the perimeter were averaged for the subsequent analysis and to determine their standard deviation. Additional measurements were taken on the round channels to determine the diameter. The diameter of the round tubes was measured in 10 circumferential locations and averaged.

The samples were characterized using a VR-5200 pattern light projection profilometer to attain surface texture attributes. An 80x magnification was selected and an overlap of 20 %. The scanned internal area of interest was approximately 38 mm long and 1.6 mm wide and reported according to ISO 25178–2:2021. An end-correction factor was applied in addition to a form correction to remove any tilt and curvature. The unfiltered primary surface texture (denoted as *primary [P]*) of the samples was evaluated in addition to the filtered roughness (denoted as *[R]*) and waviness using a λc spatial frequency cut-off filter of 0.8 mm per ISO 21920–3 guidelines. Directional profile, roughness, and waviness parameters (i.e., P*x*, R*x*, and W*x*, respectively) were also extracted from the data using a line along the center of the sample, equidistant from the edges. This directional roughness and waviness are in the direction of the flow, which also corresponds to the direction of the build. Several surface texture parameters are evaluated to characterize the samples including Sa, Sq, Sz, Sk, Spk, Spd, Pa, Ra, Rk, Wa, WP, and WPc. The full definition and mathematical definitions of surface texture parameters are provided in [2,28,35,36].

3. Results and discussion

3.1. Channel geometry characterization

Every sample was evaluated using SEM and the images of all the square channels are compiled in Fig. 5. The as-built (AB) samples

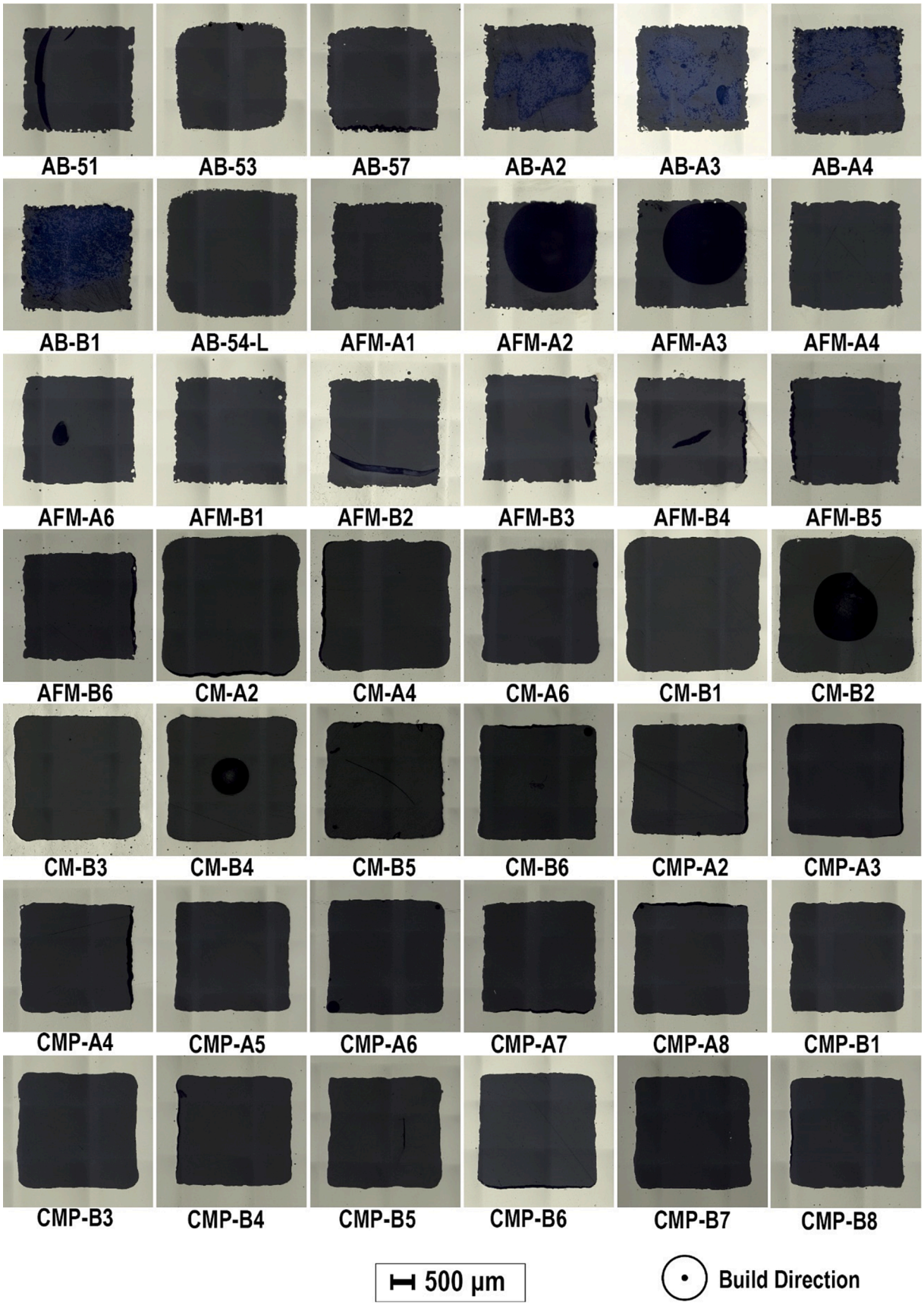

Fig. 6. Micrographs of the cross-sections of the square 615 mm channels. The cross-section is the one indicated as #2 in Fig. 4.

Table 3
Summary of the geometric data of channels obtained with caliper and cross-sectional measurements; data based on three measurements along the length of the channel.

Channel ID	Area, Avg	Perimeter, Avg	Area, Diff. from design	Perimeter, Diff. from design	Full Distance PT3-PT8	Mid Distance PT4-PT7
	mm^2	mm	%	%	mm	mm
AB-51	6.20 ± 0.064	12.81 ± 0.156	−3.9 %	26.1 %	561.87 ± 0.013	358.52 ± 0.127
AB-53	6.17 ± 0.078	13.02 ± 0.212	−4.3 %	28.1 %	562.08 ± 0.178	358.99 ± 0.216
AB-57	5.92 ± 0.073	12.08 ± 0.164	−8.2 %	18.9 %	561.67 ± 0.081	358.60 ± 0.005
AB-A2	6.31 ± 0.087	12.80 ± 0.541	−2.2 %	26.0 %	561.71 ± 0.191	358.64 ± 0.051
AB-A3	6.31 ± 0.025	13.04 ± 0.267	−2.2 %	28.4 %	561.98 ± 0.063	358.80 ± 0.025
AB-A4	6.28 ± 0.021	13.27 ± 0.418	−2.6 %	30.6 %	562.05 ± 0.013	358.71 ± 0.051
AB-B1	6.25 ± 0.093	13.27 ± 0.443	−3.2 %	30.6 %	561.75 ± 0.178	358.65 ± 0.051
AB-54-L	8.37 ± 0.186	14.38 ± 1.021	−3.6 %	22.0 %	561.47 ± 0.089	358.71 ± 0.025
AB-55-R	6.05 ± 0.125	11.73 ± 0.364	−11.2 %	26.7 %	562.09 ± 0.038	359.02 ± 0.165
AB-56-R	5.62 ± 0.035	11.85 ± 0.509	−17.6 %	28.0 %	561.76 ± 0.038	358.58 ± 0.089
AB-58-R	5.50 ± 0.100	10.85 ± 0.230	−19.3 %	17.2 %	561.75 ± 0.114	358.85 ± 0.241
AFM-A1	6.34 ± 0.064	12.44 ± 0.325	−1.8 %	22.4 %	561.80 ± 0.317	358.83 ± 0.432
AFM-A2	6.40 ± 0.013	12.42 ± 0.226	−0.9 %	22.2 %	561.57 ± 0.102	358.44 ± 0.064
AFM-A3	6.42 ± 0.032	12.17 ± 0.071	−0.5 %	19.8 %	562.15 ± 0.267	359.11 ± 0.330
AFM-A4	6.33 ± 0.091	12.00 ± 0.739	−1.9 %	18.1 %	561.72 ± 0.089	358.78 ± 0.013
AFM-A6	6.40 ± 0.088	11.65 ± 0.254	−0.9 %	14.7 %	561.90 ± 0.076	358.84 ± 0.089
AFM-B1	6.34 ± 0.028	13.28 ± 0.290	−1.7 %	30.7 %	562.10 ± 0.178	358.99 ± 0.267
AFM-B2	6.37 ± 0.027	12.50 ± 0.574	−1.3 %	23.1 %	561.78 ± 0.114	358.62 ± 0.140
AFM-B3	6.44 ± 0.053	12.17 ± 0.615	−0.1 %	19.8 %	561.91 ± 0.000	359.12 ± 0.051
AFM-B4	6.40 ± 0.023	11.81 ± 0.252	−0.8 %	16.2 %	562.08 ± 0.229	359.24 ± 0.216
AFM-B5	6.39 ± 0.141	11.92 ± 0.192	−1.0 %	17.4 %	562.18 ± 0.038	358.95 ± 0.178
AFM-B6	6.45 ± 0.014	11.39 ± 0.494	−0.1 %	12.1 %	561.85 ± 0.178	358.83 ± 0.102
CM-A2	10.25 ± 0.05	13.82 ± 0.455	58.9 %	36.0 %	562.00 ± 0.025	358.86 ± 0.013
CM-A4	8.81 ± 0.179	12.38 ± 0.282	36.5 %	21.9 %	561.92 ± 0.127	358.58 ± 0.051
CM-A6	7.16 ± 0.095	11.41 ± 0.185	11.0 %	12.3 %	561.80 ± 0.152	358.64 ± 0.013
CM-B1	9.75 ± 0.111	12.88 ± 0.093	51.1 %	26.8 %	561.84 ± 0.127	358.75 ± 0.076
CM-B2	9.81 ± 0.052	13.02 ± 0.136	52.0 %	28.2 %	561.67 ± 0.025	358.64 ± 0.013
CM-B3	8.51 ± 0.052	12.26 ± 0.108	31.9 %	20.7 %	561.67 ± 0.140	359.23 ± 0.114
CM-B4	8.51 ± 0.052	12.34 ± 0.204	31.8 %	21.5 %	562.19 ± 0.406	359.52 ± 0.483
CM-B5	7.35 ± 0.010	11.41 ± 0.058	13.9 %	12.3 %	561.85 ± 0.127	359.00 ± 0.051
CM-B6	7.37 ± 0.100	11.54 ± 0.113	14.2 %	13.5 %	562.06 ± 0.254	359.16 ± 0.203
CMP-A2	7.07 ± 0.178	11.23 ± 0.175	9.5 %	10.5 %	561.70 ± 0.127	358.80 ± 0.241
CMP-A3	7.06 ± 0.026	10.92 ± 0.142	9.5 %	7.5 %	561.59 ± 0.025	358.53 ± 0.064
CMP-A4	6.57 ± 0.041	10.85 ± 0.104	1.8 %	6.8 %	561.98 ± 0.013	358.58 ± 0.178
CMP-A5	6.77 ± 0.090	10.91 ± 0.076	4.9 %	7.4 %	561.92 ± 0.254	358.75 ± 0.191
CMP-A6	7.07 ± 0.062	11.01 ± 0.109	9.5 %	8.3 %	561.92 ± 0.076	358.90 ± 0.191
CMP-A7	6.55 ± 0.145	11.00 ± 0.074	1.5 %	8.3 %	561.59 ± 0.140	358.52 ± 0.089
CMP-A8	6.87 ± 0.028	10.78 ± 0.057	6.4 %	6.1 %	561.56 ± 0.114	358.74 ± 0.127
CMP-B1	6.74 ± 0.039	10.85 ± 0.160	4.4 %	6.8 %	561.70 ± 0.267	358.69 ± 0.152
CMP-B3	7.40 ± 0.085	11.30 ± 0.029	14.7 %	11.2 %	561.98 ± 0.305	358.74 ± 0.076
CMP-B4	6.77 ± 0.064	10.87 ± 0.168	4.9 %	7.0 %	561.92 ± 0.038	358.65 ± 0.102
CMP-B5	6.82 ± 0.105	10.94 ± 0.101	5.7 %	7.7 %	561.70 ± 0.127	358.57 ± 0.051
CMP-B6	7.28 ± 0.020	11.36 ± 0.244	12.8 %	11.8 %	561.89 ± 0.406	358.65 ± 0.216
CMP-B7	6.95 ± 0.089	10.87 ± 0.033	7.8 %	7.0 %	561.58 ± 0.089	358.60 ± 0.038
CMP-B8	6.74 ± 0.063	10.91 ± 0.060	4.5 %	7.4 %	561.66 ± 0.076	358.57 ± 0.038

indicate that adhered particles are randomly distributed on all the samples. The difference between samples fabricated with fine powder (AB-53 and AB-54-L) and the other AB samples fabricated with coarse powder is clearly visible. The fine powder covers nearly the entire surface of the sample, while the coarse powder particles cover about 30 % of the channel surface and are randomly distributed.

The SEM images for the AFM samples indicate that a high number of particles can be identified also after processing. Several of the samples such as AFM-A1, AFM-A2, AFM-B1, AFM-B2 appear to be unchanged from the AB baseline samples. In the other AFM samples, many powder particles are still present, but the peaks of the particles were removed. The remaining powder particles are still present on the material or smeared. On a limited number of AFM samples such as AFM-A4, AFM-A6, AFM-B4, AFM–B5, material is observed to be removed from the central portion or biased towards an edge. Powder particles are still present along the edges or on the side. This indicates that the process may not be completely uniform and was not as effective on longer samples.

The CM samples, shown in Fig. 5, indicate that most of the powder particles were removed. Some random particles are still present and there are indications of etching of the grains. Some indications of periodic waviness or texture can be observed, particularly on the CM-A6, CM-B5, and CM-B6 samples. Crystals can also be observed on several samples. CMP was effective at removing almost all particles. There is some evidence of macro texturing and significant etching of the grain boundaries for CMP and CM samples.

Fig. 6 displays the polished cross-sectional micrographs obtained from the #2 mid-span samples (between PT05 and PT06). These are zoomed in to show the inner wall and resulting surface from the enhancement processes. The images of the AB samples indicate high texturing around the perimeter. The coarse particles are apparent. Texturizing can be noticed on the images of the samples built with fine powder (AB-53 and AB-54-L). Samples AB-53, AB-57, AB-54-L were built without any adjacent channels, and support ribs along the mid-span, observed in Fig. 6. This caused the samples to feature slightly round corners compared to the corners of the other AB channels. Images show that most of the AFM-processed samples exhibit some partially adhered powder. The images of CM-processed samples indicate rounding of the corners and material removal from the entire inner perimeter. The cross-sectional area of the CM-processed samples is noticeably larger. Sample CM-B2 is the only one for which some loose powder is visible, and it may be a result of the sample preparation and mounting; the powder did not appear to be attached.

Fig. 6 illustrates that the CMP-processed samples now have smaller

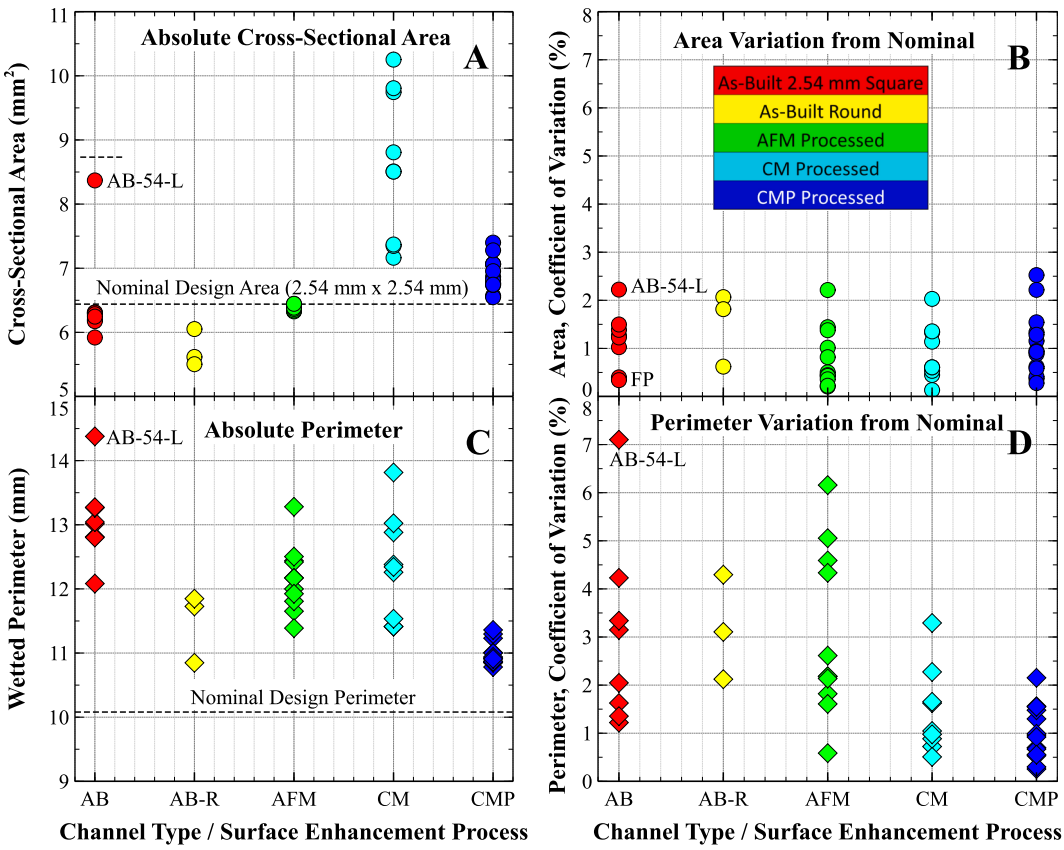

Fig. 7. Measurements characterizing the inner surface of channels. A) Cross-sectional area, B) Area Coefficient of Variation, C) Perimeter, D) Perimeter Coefficient of Variation. [FP = Fine Powder]. Symbols are colored according to the surface type or enhancement; Area and Perimeter are based on three measurements along the length of the channel.

radii compared to their previously more squared corners. The walls appear to be visually smooth. The image of sample CMP-A4 shows a potential powder particle in the upper left corner but it is not attached and likely related to polishing.

The information resulting from the analysis of the channel micrographs and from the geometric measurements is tabulated in Table 3. The data include the area and perimeter measured from the three cross-sections of each channel sample and averaged. The full perimeter was measured for each sample, and it includes all adhered powder and variations from the deposition process. The standard deviation is also provided. The difference between the measured values of the area and perimeter and the nominal (as-designed) values is also presented, together with the distances between the full and mid pressure ports with their standard deviation determined from the measurements taken different calipers. The standard deviation of the measurements features a maximum coefficient of variation of 0.043 % for the full-length measurements and 0.1 % for the mid distance measurements.

The data of Table 3 are plotted in Fig. 7 to elucidate their dependency on the channel type and surface processing methods. The values of the cross-sectional areas of the as-built channels are consistently smaller than the nominal design values due to powder adherence and shrinkage during processing (Fig. 7A). The cross-sectional areas of the AFM-processed channels are similar and closely match the nominal design values. Despite variations in slurry flow rate and pressure, the amount of material removal appears to be limited. Increasing the flow rate and pressure of processes using abrasive/slurry media may be necessary to enlarge the channel area. CM-processed channels cause significantly larger values of the cross-sectional area compared to the as-built value and the nominal design value, as previously observed. The CMP samples indicate consistent areas and perimeters despite processing parameter variations.

Fig. 7C reports the values of measured perimeters depending on the post-processing treatment. As expected, the perimeter value of as-built samples is higher than the design value (i.e., an ideal value formed by perfectly straight segments), which is 10.16 mm for most samples. The AB-54-L sample was designed with a nominal perimeter of 11.79 mm. The perimeter value of as-built round samples (9.017 mm) similarly deviate from the nominal design values. AFM samples feature a higher perimeter value, similar to the value of as-built samples, due to the presence of residual powder particles. The larger value of the area of CM samples results from the higher amount of removed material, which effectively eliminates adhered powder and even some of the underlying surface. CMP processing effectively removes particles while keeping to a minimum material removal, allowing for more precisely controlling the value of the area and perimeter. The data sets of Fig. 7C indicate that the CMP process can effectively reduce and planarize the perimeter with minimal area increase.

Fig. 7B shows values of the coefficient of variation (CV) for the area of each channel type, while Fig. 7D displays the value of CV for the perimeter. The CV, calculated as the standard deviation divided by the mean, indicates the variance between cross-sections along the length of the channel. The areas and perimeters are based on the average of three cross-sections, with the means presented in Fig. 7A and Fig. 7C, respectively. This CV is a merit parameter measuring the capability of surface enhancement processes in producing consistent uniform area and perimeter along the channel length. A high CV suggests significant variation.

Regardless of the surface enhancement process, the value of CV for the area along the channel lengths remains within 2.5 %. This variation accounts for both the effects of surface processing and measurement error, indicating consistent processing conditions. The area of the AFM samples vary by 2.2 % along their length, despite having nearly identical

Table 4
Summary of the measured values of parameters identifying surface texture, roughness, and waviness. [P] is the *primary* texture and [R] denotes the *filtered roughness* texture.

Channel ID	Sa [P]	Sq [P]	Sp [P]	Sv [P]	Sk [P]	Spk [P]	Sa [R]	Wp	Wa	Pa	Ra	Rk
	µm	µm	µm	µm	µm	µm	µm	µm	µm	µm	µm	µm
95 % C.I. (±)	**0.12**	**0.12**	**33.9**	**1.98**	**0.54**	**0.39**	**0.09**	**2.16**	**0.73**	**1.09**	**0.42**	**1.57**
AB-51	23.3	29.9	275.2	186.1	71.3	38.9	18.6	49.2	13.0	22.7	15.3	44.6
AB-53	17.4	21.9	119.2	122.2	55.8	20.6	12.5	30.5	8.9	16.2	11.3	36.7
AB-57	31.6	40.3	226.9	313.2	99.8	41.2	22.2	63.8	19.2	31.4	19.3	54.7
AB-A2	28.4	37.1	279.0	304.5	85.0	47.9	20.4	68.7	14.4	23.7	16.4	43.9
AB-A3	29.2	37.6	341.8	260.9	89.2	45.8	22.3	47.6	13.2	24.3	18.3	49.5
AB-A4	31.2	40.5	327.8	284.6	94.9	56.4	20.4	49.2	13.0	23.2	16.1	44.6
AB-B1	28.2	37.3	318.1	269.2	87.2	47.6	21.8	74.0	14.4	26.0	18.9	54.4
AB-54-L	18.1	22.9	128.8	145.5	57.9	22.5	12.7	32.3	9.4	17.5	11.8	39.1
AB-55-R	15.5	20.5	105.2	133.3	46.3	18.3	11.3	24.8	9.0	14.2	9.8	30.3
AB-56-R	28.2	36.8	171.1	244.0	83.7	40.2	22.1	61.6	16.5	28.1	18.4	53.0
AB-58-R	32.3	41.8	177.1	444.4	96.9	49.8	26.1	85.0	19.8	30.7	18.3	54.0
AFM-A1	29.0	36.8	196.0	360.3	90.9	43.4	20.1	33.4	11.5	22.6	15.4	44.0
AFM-A2	26.6	34.3	338.9	199.4	83.7	45.7	19.3	49.4	16.0	23.3	15.5	48.0
AFM-A3	25.8	34.2	303.3	239.9	80.3	47.1	19.5	41.5	12.2	22.6	15.6	48.1
AFM-A4	26.3	34.4	281.3	309.6	79.8	46.0	19.1	39.0	12.6	22.0	14.9	44.2
AFM-A6	27.6	36.9	284.4	279.3	73.2	58.8	14.1	33.4	11.5	17.0	9.7	29.3
AFM-B1	26.9	34.9	340.7	330.4	81.9	41.5	20.4	49.4	16.0	25.0	17.1	48.3
AFM-B2	25.3	32.8	283.1	236.9	76.6	38.3	20.4	41.5	12.2	22.2	16.0	46.4
AFM-B3	22.5	29.5	243.2	301.5	70.0	34.9	18.3	34.3	11.5	19.4	13.2	39.1
AFM-B4	20.9	27.5	292.4	259.0	63.8	33.4	16.5	34.6	10.3	17.5	11.7	35.2
AFM-B5	22.6	30.0	384.0	248.5	66.1	40.3	16.8	37.4	11.0	18.8	11.9	35.7
AFM-B6	21.4	28.3	333.1	262.2	62.7	39.7	16.1	32.4	10.2	17.0	11.7	34.2
CM-A2	12.4	16.0	262.5	222.1	39.0	14.0	6.7	21.1	8.2	10.0	4.2	12.1
CM-A4	13.5	18.2	140.6	280.0	39.9	13.0	8.8	26.2	9.1	12.7	6.0	16.9
CM-A6	15.1	19.4	110.5	232.1	47.4	19.0	11.6	29.7	8.7	14.0	9.0	28.4
CM-B1	14.3	18.5	104.9	220.5	43.5	12.4	7.0	22.9	11.2	12.1	4.9	13.8
CM-B2	12.2	15.7	89.4	174.8	37.2	12.9	6.3	20.5	7.8	9.1	4.4	13.2
CM-B3	11.3	15.2	165.9	199.4	33.9	12.3	7.6	22.8	7.8	10.2	5.7	15.6
CM-B4	12.6	16.5	84.4	202.8	37.6	12.9	7.4	22.3	8.6	10.5	5.4	15.8
CM-B5	13.1	17.4	290.4	186.9	40.5	19.3	8.9	31.9	8.3	12.2	7.3	23.1
CM-B6	13.7	17.7	169.9	229.3	42.7	14.0	9.1	25.1	8.1	13.0	7.2	22.3
CMP-A2	12.7	16.4	426.4	137.7	41.0	15.4	6.8	28.4	10.6	11.9	5.1	16.0
CMP-A3	11.8	15.0	155.5	130.9	35.8	19.7	5.3	27.2	8.3	9.9	3.6	11.1
CMP-A4	14.0	17.7	165.0	189.5	44.9	19.7	8.6	27.9	8.6	12.4	6.7	21.5
CMP-A5	13.0	17.0	146.0	348.8	41.0	16.8	10.3	29.2	9.1	11.7	5.7	17.4
CMP-A6	12.8	16.7	172.8	123.0	38.8	23.9	6.5	22.7	8.0	10.1	4.8	15.8
CMP-A7	18.6	23.3	89.0	189.2	59.6	24.1	10.6	40.3	12.9	16.5	8.3	25.6
CMP-A8	17.0	21.7	285.2	162.6	52.1	26.4	7.1	35.9	10.0	12.2	5.1	16.2
CMP-B1	16.4	20.7	135.1	168.6	52.1	19.8	9.4	36.9	12.3	15.2	6.8	22.1
CMP-B3	15.6	21.3	259.4	308.1	48.3	25.5	6.5	28.5	10.6	12.1	3.7	11.5
CMP-B4	15.6	20.0	151.7	148.6	48.8	23.5	9.9	39.2	11.0	15.5	7.5	24.1
CMP-B5	14.1	18.6	235.7	338.1	43.4	23.6	8.5	34.1	10.3	13.0	5.8	18.2
CMP-B6	15.3	19.4	112.1	101.3	48.8	24.1	6.5	44.0	11.6	13.2	4.6	14.4
CMP-B7	11.9	15.5	118.8	184.1	36.2	17.3	7.1	24.7	8.4	10.8	5.4	16.6
CMP-B8	15.7	22.0	279.7	221.0	48.6	31.3	10.2	38.6	10.0	14.4	7.3	20.8

absolute cross-sectional areas.

The perimeter CV range is higher than the cross-sectional area CV range, as shown in Fig. 7D. No clear trends link perimeter CV to area CV; variations appear as random error (Refer to Supplemental). As-built samples with randomly adhered powder show consistent area and perimeter variation along the length. AFM processed samples exhibit the highest CV due to processing inconsistencies, with some powder remaining adhered to the walls while other areas are cleared, leading to a higher perimeter variation (5.6 %). CM samples demonstrate consistent perimeter measurements along the channel length, with a CV within 3.3 %. The CMP process shows excellent consistency, maintaining perimeter variations within 2.2 % along the channel length.

3.2. Surface texture characterization

All samples were scanned to obtain quantitative information on the surface texture at the mid-point of the channels as indicated in Fig. 4. The scans provided the amplitude of the primary and roughness areal texture, spatial, functional, hybrid, and material ratio parameters shown in Table 4. Additionally, the 2D profile, roughness, and waviness parameters were obtained along the centerline of the channel.

The 95 % confidence interval (C.I.) of the values was obtained by repeating four times the measurements characterizing a single as-built sample. Reporting values related to the as-built sample introduces bias in the confidence interval for parameters associated with single-point high peaks and due to the powder particles, such as Sp. The confidence interval characterizing samples with enhanced surface texture is likely much higher (>95 %). Additionally, directional measurements (Wa, Ra, Pa) are affected by much larger deviation, as slight changes in line placement can result in significant variations of peak height or valley lengths. In contrast, areal measurements are affected by lower deviation since all texture artifacts of the measured area comprise the calculated value (i.e, Sa, Sq, Sp, etc). As noted, the Sp value is based on a single peak value across the entire surface therefore bound to be biased towards higher values and a higher standard deviation. This issue underscores the importance of using a merit parameter such as reduced peak height (Spk) and core roughness (Sk).

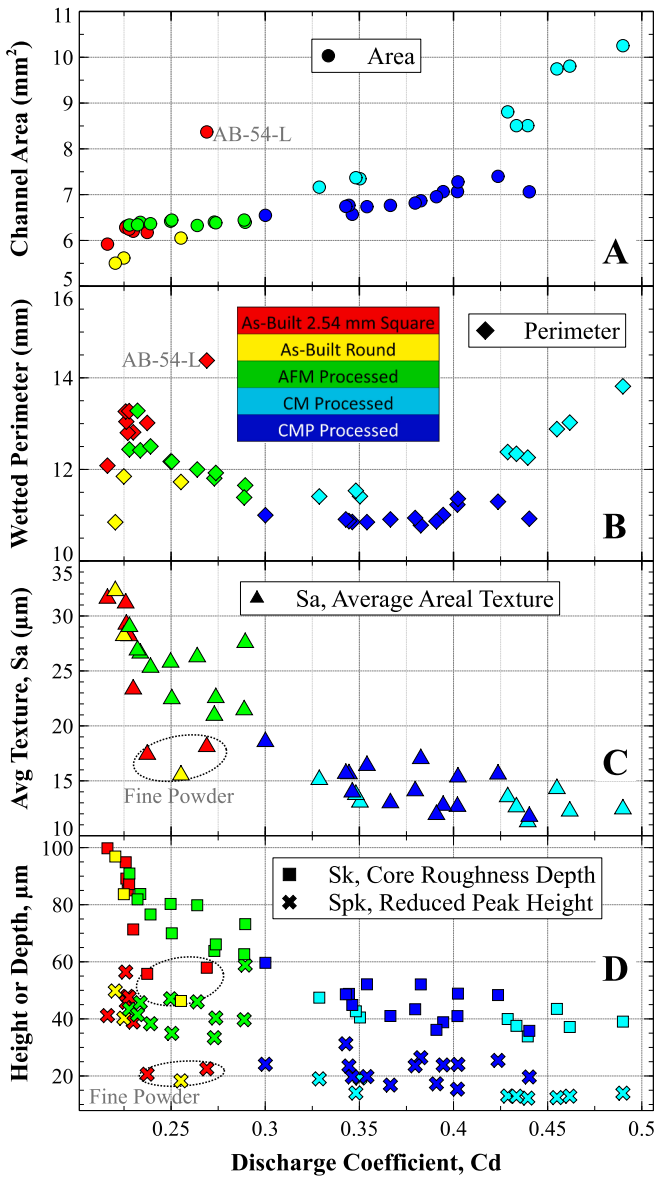

Fig. 8. Relationship of the estimated *Cd* with A) Measured cross-sectional area, B) Measured perimeter, C) Measured average primary texture, and D) Sk and Spk. The color of the symbols is associated to the surface enhancement process as listed in the legend.

3.3. Discharge coefficient

The discharge coefficient was calculated according to its definition, namely

$$Cd = \frac{\dot{m}}{A\sqrt{2\rho\Delta P}} \tag{4}$$

where $\dot{m}$ is mass flow rate in kg/sec, A is area in mm^2, ρ is density of water in grams/cm^3, and ΔP is the differential pressure between PT08–PT03 in bar. The discharge coefficient was evaluated for each channel sample at each test pressure. The area is based on the average of three measurements (shown in Fig. 4) and listed in Table 3.

Fig. 8 shows the functional relationship between *Cd* and the cross-sectional area, perimeter and the average primary texture. The effect of surface enhancement processes on flow resistance is similar, with CM and CMP causing the lowest resistance (highest *Cd*). The *Cd* increases with the cross-sectional area, as expected. The large square as-built channel (AB-54-L) features an area that is nearly identical to that of channels CM-B3 and CM-B4 and its average *Cd* is 38 % lower. The *Cd* of the large as-built AB-54-L channel is higher therefore the flow resistance is lower than that of the as-built channels featuring smaller cross-sectional area, as expected. A slight difference in flow resistance can be observed between AB channels with the larger and smaller cross-sectional area, which suggest that other factors, such as the texture, have a higher influence on the flow resistance.

Fig. 8 also shows that the value of *Cd* increases with decreasing perimeter lengths down to $Cd = 0.3$. For a range of perimeter values, it remains constant and equal to approximately 0.3, then increases again starting from $Cd = 0.4$. This is expected since the powder adherence and surface undulations cause the value of the perimeter to increase at lower Cd values. The decrease of the perimeter value for *Cd* in the range from 0.2 to 0.3 is due to the full removal or partial removal of powder particles with sizes lower than the average particle size (73 µm). The larger perimeter values associated with values of *Cd* higher than 0.4 is mostly due to the increase in the channel cross-sectional area resulting from material removal.

Fig. 8C displays how the flow resistance decreases exponentially with decreasing values of the average areal texture (primary), Sa. The Sa strongly decreases down to $\sim Cd = 0.32$, while for larger values of *Cd* it decreases very slightly for values of from $Cd = 0.32$ up to 0.5. Using the core texture depth (Sk) and reduced peak height (Spk) parameters allow for better discernment of the average distance between peaks and valleys, thus filtering out the maximum heights of peaks and valleys [4]. Fig. 8D shows how Sk and Spk vary with *Cd*. As the core peak-to-valley depth reduces, the *Cd* increases. The value of Sk becomes approximately constant for heights of peaks or valleys of ~ 50 µm, and it weakly decreases for values of *Cd* up to 0.5. The trend of Spk is similar, although not as pronounced. Overall Sk and Spk decrease exponentially with *Cd*.

It can be concluded that flow resistance depends for the most part from roughness-related peaks and their density, as well as from the planarization of waviness and their density. Fig. 9 presents the summary of the relations between Cd and Spk, Spd, Wp, and WPc and the cross-sectional area. Given that material is removed from the surface due to the enhancement treatment, the resulting channel cross-sectional area is larger and Spk is lower. Compared to the Spk of the as-built channels (AB-xx), the Spk of channels whose surfaces are treated is lower by 79 %, and the density of these peaks (Spd) is lower by 74 %. Similar results hold for waviness, with Wp and WPc being lower by 76 %. The calculated Reynolds number indicates that the channels operate in the turbulent regime. Higher micro peaks, macro waviness, and their density distribution along the channel length increase boundary layer turbulence and fluid dynamic losses. Effective removal of these features is crucial for reducing flow resistance.

To better estimate the amount of material removal required to obtain a specified flow resistance, Fig. 10 provides the visualization of the relationship between material removal (MR) per side and Sk, Spk, and Wp. MR per side is calculated based on the simplifying assumption that

$$MR = \frac{\sqrt{A_{Ch}} - \sqrt{A_{AB}}}{2} \tag{5}$$

where A_{Ch} is the average cross-sectional area of the channel calculated measured at three locations and A_{AB} is the value of the average as-built area. The results in Fig. 10 suggest that removing powder of the minimum size (diameter of 45 µm) is required to reduce the flow resistance by approximately 40 %, but to reduce flow resistance by > 75 % the powder of maximum size (105 µm) must be removed. The removal of large-size powder eliminates all the adhered powder particles and decreases flow friction within the boundary layer.

3.4. Differential pressure and friction factor

In order to calculate the Colebrook-White friction factor using existing methods, Reynolds number, pressure difference and hydraulic

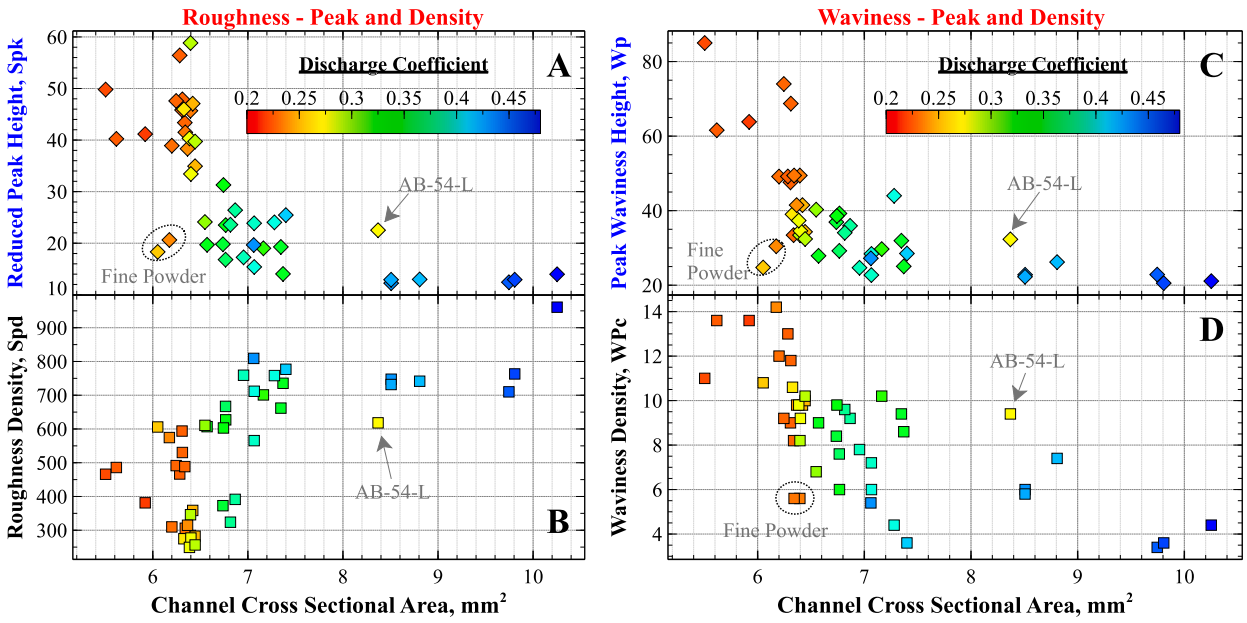

Fig. 9. Flow resistance dependence for roughness and waviness of all the tested channels: A) Spk, B) Spd density, C) Wp, and D) WPc density.

diameter (D_h) [37] must be determined. According to conventional methods, all these calculations assume a circular tube and methods to convert these quantitates for the case of non-circular geometry are documented in several publications [38–40]. The conventional definition of hydraulic diameter for a square channel is

$$D_h = \frac{4A}{P} \tag{6}$$

where A is the area in mm^2 and P is the wetted perimeter in mm. The hydraulic diameter was calculated according to equation (6) for all channels and values are reported as black triangles on the plot of Fig. 11. This figure shows that values of D_h calculated with equation (6) depart significantly from the expected linear relation between area and perimeter for samples featuring small values of the area and comparatively large value of perimeter. Channels with as-built surfaces have a measured perimeter approximately 30 % greater than the nominally designed channel with smooth walls. The plot of Fig. 11 shows that the deviation from linearity is significant for the points referring to as-built and AFM channels with cross-sectional areas less than 6.8 mm^2. In those cases, the value of the perimeter is much larger than the nominal value due to the surface texture resulting from the adhered powder and waviness, yielding a value of the D_h which deviates from the one given by the linear trend by around 18 %.

Other issues affect the deviation from the linear dependence of D_h. First, the perimeter exhibits a higher coefficient of variation (CV) compared to the CV of the cross-sectional area (see Fig. 7), introducing additional uncertainty in the D_h values. Second, using D_h with large perimeter values could further bias the estimation of the friction factor. Since sand grain roughness is already incorporated into the friction factor correlation, accounting for the increased perimeter due to high roughness would effectively result in “double bookkeeping” of the texture values.

Given the unsatisfactory ability of the conventional definition of hydraulic diameter of correlating the cross-sectional area and the perimeter of the additively manufactured channels, an alternative definition D_h evaluated for a square cross-section channel is

$$D_{h1} = \sqrt{A_{meas}} \tag{7}$$

where A_{meas} is the measured cross-sectional area, whose values for the considered channels are listed in Table 3. The justification for this definition is that the D_h for a square channel is simply the length of a side [11], as previously mentioned. Values of D_{h1} are shown as white circles in Fig. 11 together with their correlating function displayed as a dotted line. The values of D_h, associated with an area larger than 6.6 mm^2, form a linear function and the values of D_{h1} appear to be offset from this. This observation leads to a definition of hydraulic diameter valid for square channels that includes a texture attribute, namely

$$D_{h2} = \sqrt{A_{meas}} - 2Sk \tag{8}$$

where Sk is the core texture height. This definition of hydraulic diameter incorporating a correction term twice the surface texture attribute is similar to definitions for determining a representative cross-sectional area in AM mechanical testing [41,42] and also adopted in constricted flow theory presented by Taylor et al. [10,43]. The introduction of a texture correction term eliminates the bias resulting from the case of a highly texture perimeter: channels with high texturing (those with a cross-sectional area lower than 6.6 mm^2) feature values of D_h that are 17 % lower, with a value of the cross-sectional area which is 4.5 % lower. For this reason, the definition of hydraulic diameter provided by Equation (8) is adopted for all the calculations. The ratio of length (PT08-PT03) to hydraulic diameter is approximately 179:1.

After an appropriate hydraulic diameter is calculated for the square channels, the Reynolds number is determined. The Reynolds number is defined as

$$Re = \frac{D_{h2} v \rho}{\mu}, \tag{9}$$

where D_{h2} is calculated according to equation (8), v is computed from equation (3), ρ is the fluid density, and μ is defined according to equation (1).

The values of Re for all test runs range from 17,011 to 122,818, thus the flow is fully turbulent. Fig. 12D provides a plot of the values of the Reynolds number as a function of the mass flow rate with the symbols colored according to the velocity range. Values referring to samples treated with surface enhancements (polished) are plotted along with those referring to the as–built samples obtained with coarse powder and fine powder.

Fig. 12E displays a chart of the pressure drop measured as the pressure difference between the values recorded by the PT08 and PT03 sensor as a function of the measured $\dot{m}$. The symbols are colored according to the processing method with which each channel was treated.

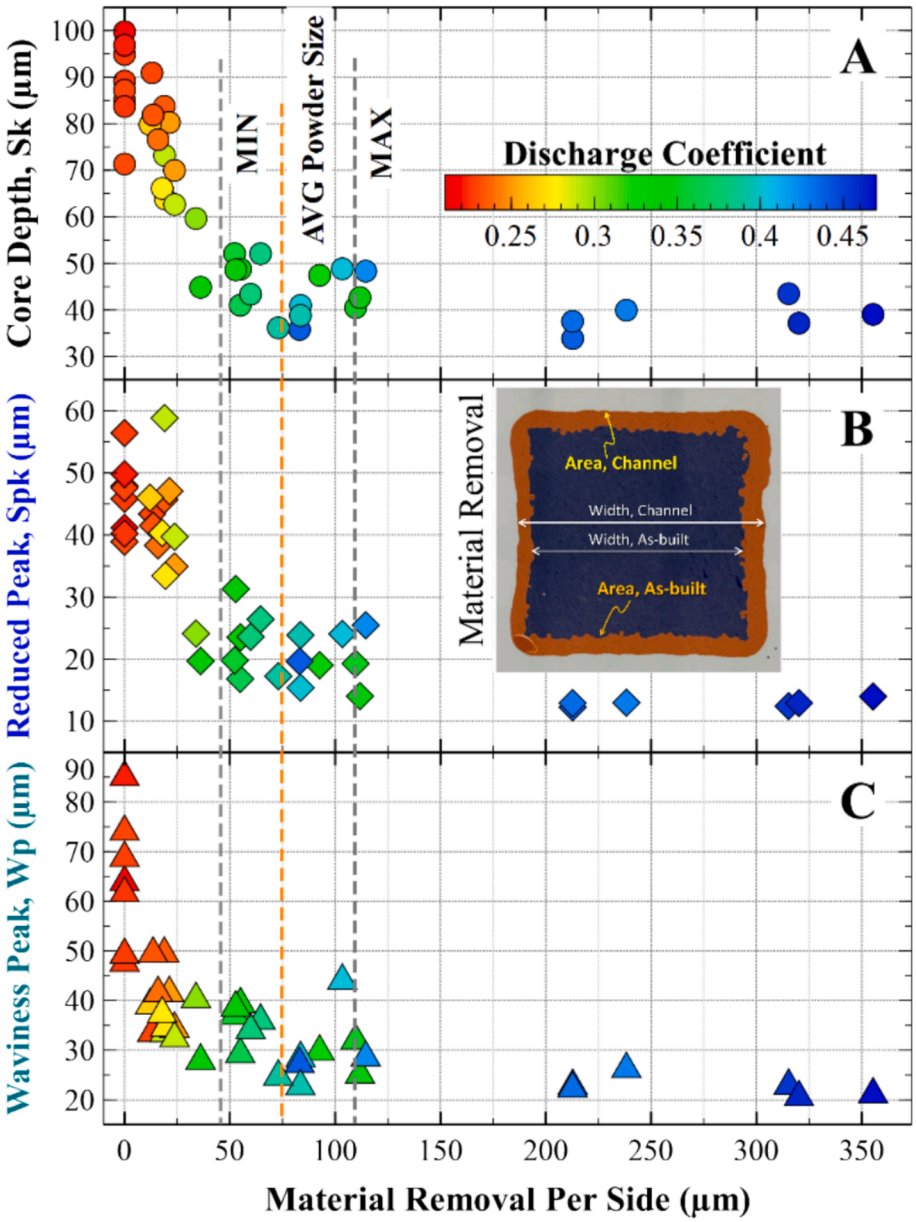

Fig. 10. Relationship between material removal per side based on: A) Core Depth, Sk, B) Reduced Peak Height, Spk, and C) Waviness peak height, Wp.

As expected, differential pressure measured for the as-built channels are the highest for all mass flow rates. The AB-54L channel features a larger cross-sectional area, therefore the pressure drop measured for this channel is lower than that measured for the other as-built samples. The values of differential pressure at approximately constant mass flow rate equal to 0.069, 0.095, and 0.13 kg/sec were measured during test runs in which the venturi flow meter was employed. The value of $\dot{m}$ is the maximum due to the resistance in the channels and lower differential pressure.

Fig. 12, plots A, B, C, indicate the relation between pressure drop and mass flow rate is also displayed as a function of core surface texture, average directional waviness, and average directional roughness. Also the results related to average texture, Sa, were analyzed, but the trends are similar to those valid for Sk, whereby the only difference is the range of values, namely from 11 to 32 µm. The trends visualized in Fig. 12 for surface texture, waviness, and roughness are generally as expected. Values related to the surfaces with the highest roughness and waviness correlate with the highest pressure drop and vice versa. The core texture depth, Sk, is primary therefore it encompasses the effect of the waviness and roughness surface attributes. The plots indicate that both roughness and waviness affect the flow resistance, although the effect of roughness is much stronger. This observation is corroborated by the analysis of the *Cd* trends presented in Section 3.3.

The correlation to determine pressure loss along the length of the channels and valid only in case of turbulent flow requires a correlation for the friction factor. The empirical Colebrook-White equation for the friction factor f_c [8,9] is

$$\frac{1}{\sqrt{f_C}} = -2log_{10}\left(\frac{2.51}{Re\sqrt{f_C}} + \frac{K_s}{3.7D_{h2}}\right) \tag{10}$$

where Re is defined by Equation (9) and K_s is the equivalent sand grain roughness, sometimes referred to as ε. Equation (10) requires an implicit method to determine f_C.

Moody obtained a well-known diagram based on measurements performed by Darcy and Nikuradse showing the relationship between Reynolds number and friction factor depending on a relative pipe roughness [5]. The diagram was intended to provide designers with a

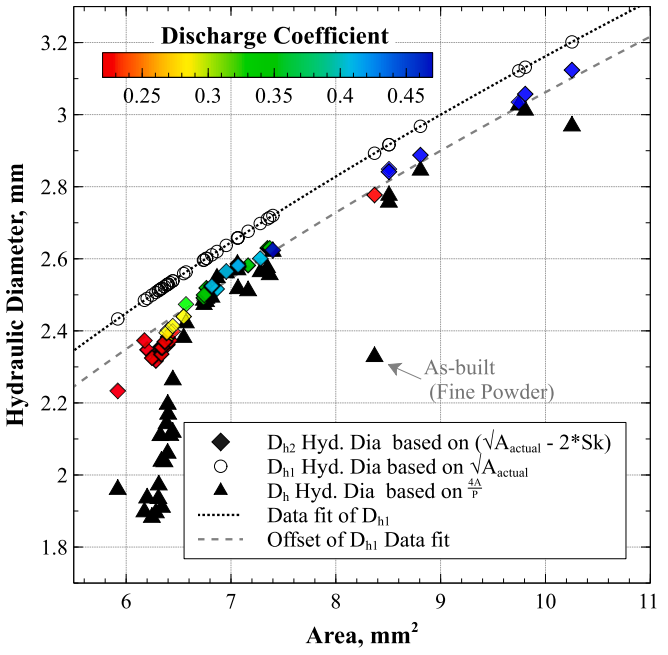

Fig. 11. Hydraulic Diameter based on various definitions. D_{h2} is defined by equation (6), D_{h1} is defined by equation (7), and D_h is defined by equation (8). The D_{h2} symbols are colored according to the value of the Cd.

graphic-based means to obtain values of friction factor for analysis. Several implicit and explicit equations to calculate the friction factor were developed, based on the Moody diagram and other experimental data sets. A commonly adopted explicit equation based on the Moody diagram for the calculation of the friction factor, defined here as f_M, is [37]

$$f_M = 1.14 + 2\log_{10}\left(\frac{D_{h2}}{K_s}\right)^{-2} \tag{11}$$

The ratio K_s/D_h in equation (10) (and its inverse in equation (11) is commonly known as *relative pipe roughness* and it can be determined from the Moody diagram. The K_s/D_h ratio defines the sand grain roughness relative to the hydraulic diameter of the channel or pipe. Other researchers have proposed explicit expressions of the friction factor [37,44]. These expressions can vary depending on the range of Reynolds number, thus flow regime, and on the K_s/D ratio. The Swamee and Jain explicit friction factor expression [45] is recommended for values of $K_s/D \leq 0.05$ and is given by

$$f_S = \frac{0.25}{\left[\log\left(\frac{\frac{K_s}{D_{h2}}}{3.7} + \frac{5.74}{Re^{0.9}}\right)\right]^2}, \tag{12}$$

where Re is defined from 7.12. Mileikovskyi and Tkachenko introduced another expression for the friction factor [46], valid for a wider range of K_s/D values, up to 0.65, and for Re up to 10^9. This expression for the friction factor, defined in this case as f_T, is

$$f_T = \frac{1}{\left[0.8284 ln\left(\frac{\frac{K_s}{D_{h2}}}{4.913} + \frac{10.31}{Re}\right)\right]^2} \tag{13}$$

The expression of Brkic and Cojbasic [47] is

$$f_B = \left[-2log\left(\frac{2.18B}{Re} + \frac{\frac{K_s}{D_{h2}}}{3.71}\right)\right]^{-2}, \tag{14}$$

where B is

$$B = ln\frac{Re}{1.1816\ln\left(\frac{1.1Re}{\ln(1+1.1Re)}\right)}. \tag{15}$$

Finally, Avci and Kargoz [48] suggested to evaluate the friction factor, termed f_A, as

$$f_A = \frac{6.4}{\left[ln(Re) - \ln(1 + .01Re\frac{K_s}{D_{h2}}\left(1 + 10\sqrt{\frac{K_s}{D_{h2}}}\right))\right]^{2.4}}. \tag{16}$$

The validity of these friction factor definitions were experimentally evaluated with a general focus on round pipes [49,50]. One of the objectives of the experiments presented here is to characterize and determine an explicit friction factor expression for the analysis of additively manufactured square channels, with large variations in the surface texture.

All the expressions for the friction factor were compared regarding predictions of the differential pressure over the square-section channels, and the Darcy friction factor

$$f_D = \frac{2\Delta P g_c D_{h2}}{\rho L v^2}. \tag{17}$$

In equation (17), ΔP is the pressure difference between two measuring ports, v is given by Equation (3), ρ is the fluid density, g_c is the gravitational constant (9.81 m/sec^2), and L is the length between the locations of the considered ports. Fig. 13 depicts how the Darcy friction factor, determined by correlating all the measured the differential pressure data, varies with the mass flow rate. As expected, for low values of the mass flow rate f_D increases for a given of mass flow rate. f_D is larger for the AB channels and the AFM channels, for which a high density of powder particles are present on the surface. Fig. 13 shows the constant mass flow rate tests conducted at 0.069, 0.095, and 0.13 kg/s, along with data sets where the flow rate is maximized. The friction factor remains relatively constant regardless of the flow rate. The values of f_D for selected channels is represented by a horizontal line, indicating minimal variation in friction factor with changes in flow rate (Supplemental).

The values of the Darcy friction factor obtained by correlating experimental results was evaluated against the values of friction factor calculated with the expressions based on the surface texture (Re, K_S, and D_{h2}) in relation to the discharge coefficient (Fig. 14). These data are derived using the full–length channel value of the differential pressure (PT08-PT03) for each test condition. None of the friction factor correlations obtained with Equations (10) through (16) match the values of Darcy friction factor derived from measurements. The values obtained with Equations (10) through (16) show similar trends across the range of Cd with a maximum deviation between predictions of 10 %. The value calculated with the Colebrook-White correlation falls within the median range of the values calculated with the other correlations. The plot also shows that there is discrepancy between values calculated with all the friction factor correlations and the Darcy friction factor, with the value calculated with surface-based friction factor correlations being lower for values of $Cd < 0.27$ and higher for $Cd > 0.3$. Based on these considerations, the Moody-derived friction factor expression (f_M) was selected for further analysis. At lower flow resistances, values calculated with f_M feature the least variance from those calculated with the f_D expression. At higher flow resistances, values calculated with the f_M *correlation* are close to the mean of values computed with all other friction factor expressions.

The friction factor correlations depend on the surface roughness and

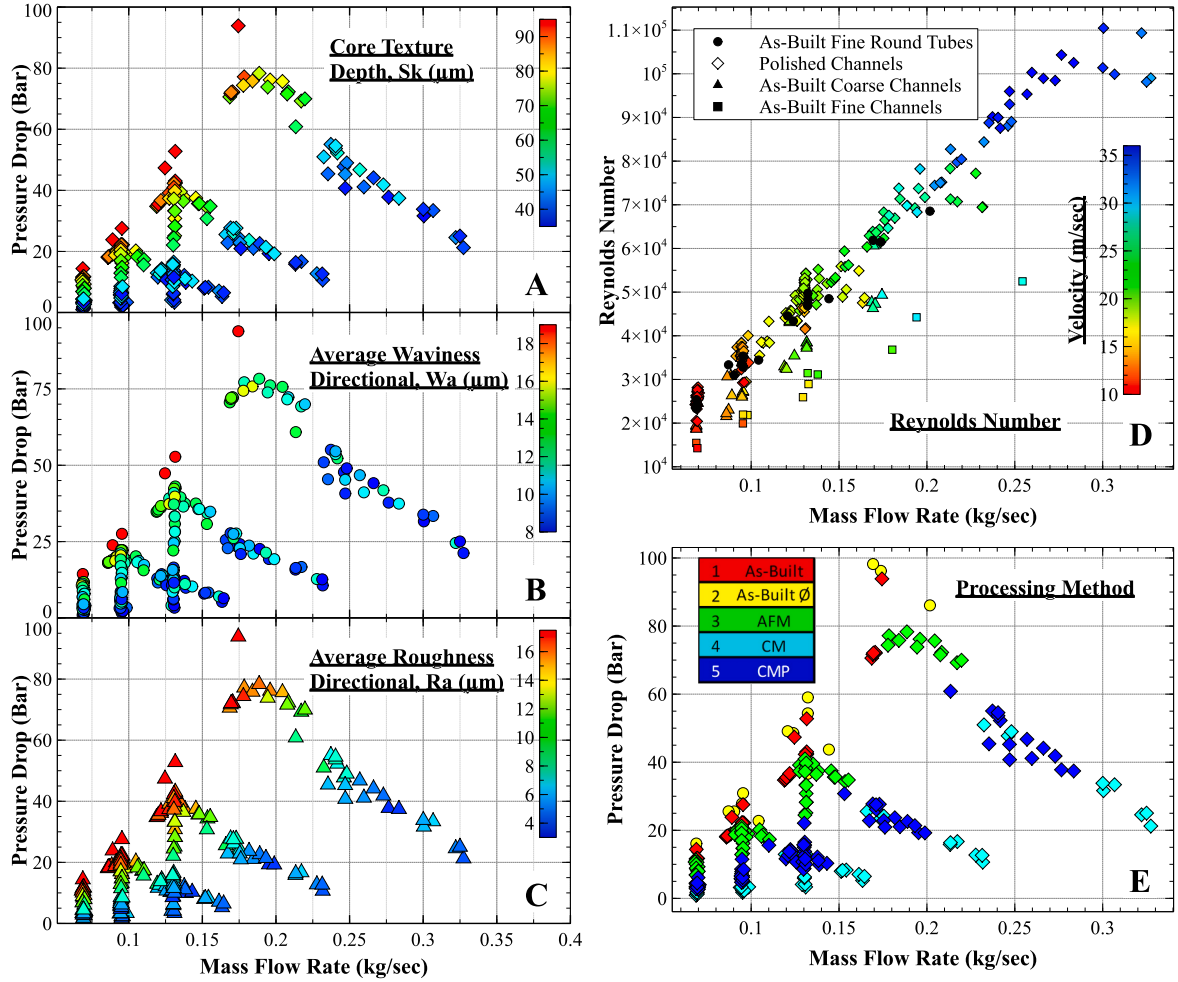

Fig. 12. Mass flow rate compared to A) Pressure drop colored by Sk, B) Pressure drop colored by Wa, C) Pressure drop colored by directional Ra, D) Reynolds number colored by velocity and E) Pressure drop colored by processing method.

channel hydraulic diameter (K_s, D_{h2}) along with Re. K_s is not representative of surface roughness, or of surface texture, which can be directly measured. A possible assumption for the evaluation of surface roughness is that it is defined as the average directional roughness, Ra, since this is the most commonly measured. However, this parameter is insufficient to fully characterize texture, and other surface texture attributes are discussed in Section 3.5. Adams et al. [51] proposed a constant value of 5.863 for the K_s/Ra ratio. Similarly, Forster recommended a value of 7 for K_s/Ra [52], while Koch and Smith suggested a value of 6 [53]. The value of 5.863 was initially used to convert *Ra* to a *Ks* for the data presented in Fig. 14. However, other authors have argued that a single K_s parameter is insufficient [44,54]. This deficiency is evident in Fig. 14 where variations in surface texture lead to changes in flow resistance and deviations in the friction factor correlations compared to the f_D correlation.

The correct characterization of the roughness of a surface is crucial for determining differential pressure along fully turbulent flow through a channel because the viscous sublayer and roughness sublayer are disturbed and deflected by the surface texture. The height and spacing of the roughness and waviness alters the contribution to the drag and pressure losses in addition go thickening the boundary layer further constricting the flow. Fig. 15 shows that similar values of differential pressure may result from largely different Reynolds numbers and velocity values. This observation is consistent with that of Kadivar et al. [44], who noted that pressure drop remains unaffected by fluid viscosity and velocity when the surface texture peaks penetrate the roughness sublayer. The height of the roughness sublayer can be as much as 2 to 5 times the diameter of the sand grain roughness, K_s [55]. The surface texture that results in the K_s is complex and comprises both micro roughness and macro waviness [4], therefore these surfaces must be fully characterized, and new correlations determined.

3.5. Sand grain roughness

The definition of sand grain roughness is related to the experiments of Darcy and Nikuradse: sand was bonded to internal pipes using an adhesive or lacquer in order to obtain a prescribed level of internal surface roughness [6,7]. The exact cross-sectional surface texture from these experiments is not known, but they are commonly represented as shown in Fig. 16 (left). The surface roughness was obtained by measuring the diameter of a sand grain or evaluated by means of contact-type profilometers. Capillary action between the lacquer and sand grains applied to the pipe surface likely created small radii and captured the sand grains, so using the sand grain diameter is also an incorrect hypothesis. While sand grain roughness may appear similar to the roughness of a surface resulting from additive manufacturing, as in the case of a surface generated with the LP-DED process with its adhered powder particles, experimental data sets [44] indicate that the two surfaces are quite different, as evident from the images of Fig. 16 (right). The microscopic shape of the surface resulting from the LP-DED process is made of both smooth and sharp irregularities due to waviness and roughness, and a combination of both. The resulting flow from these irregularities can result in trapped eddies at sharp transitions or pockets, vortex shedding, and crests that protrude into the boundary layer [56].

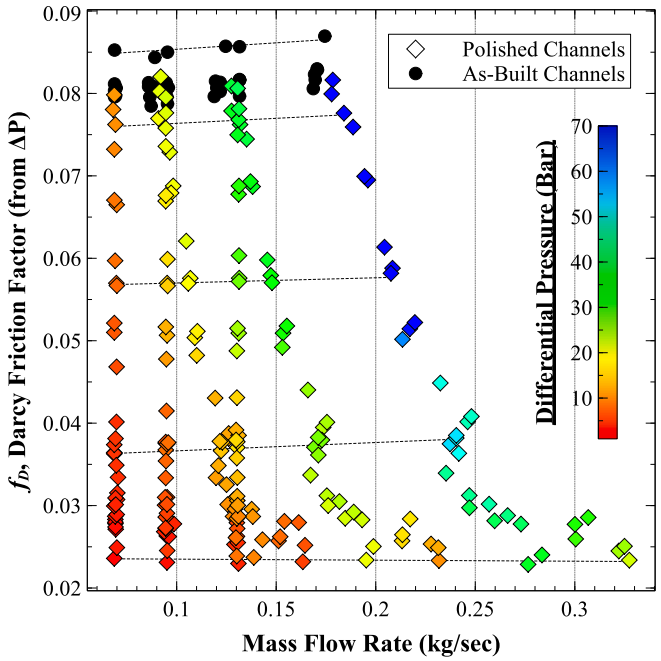

Fig. 13. Darcy friction factor as a function of mass flow rate. The dotted horizontal lines represent the same channel across the six different test runs. The points are colored according to the measured value of the pressure difference between pressure ports.

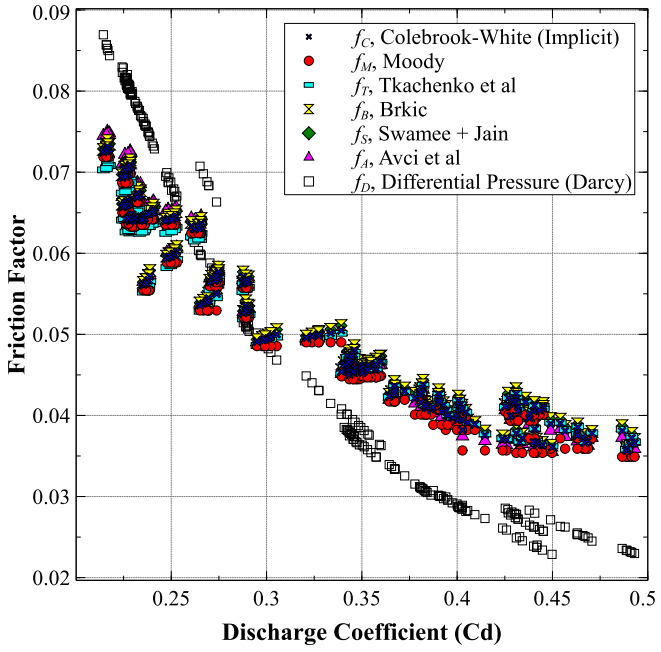

Fig. 14. Comparison of the friction factor determined experimentally from differential pressure measurements along with friction factors calculated from various correlations (Equations (10) to (16).

The reason for the deviation between values of the friction factor computed with predictive equations and those based on measured differential pressures is further elucidated with the help of Fig. 17, indicating the percent deviation in the friction factor (Δf) at three fixed flow rates. As the differential pressure increases due to the velocity rise from the increased mass flow, the experimental friction factor remains nearly constant across each channel. The maximum coefficient of variation (CV) of f_D at the three fixed flow rates is 5.8 %. The average CV across all

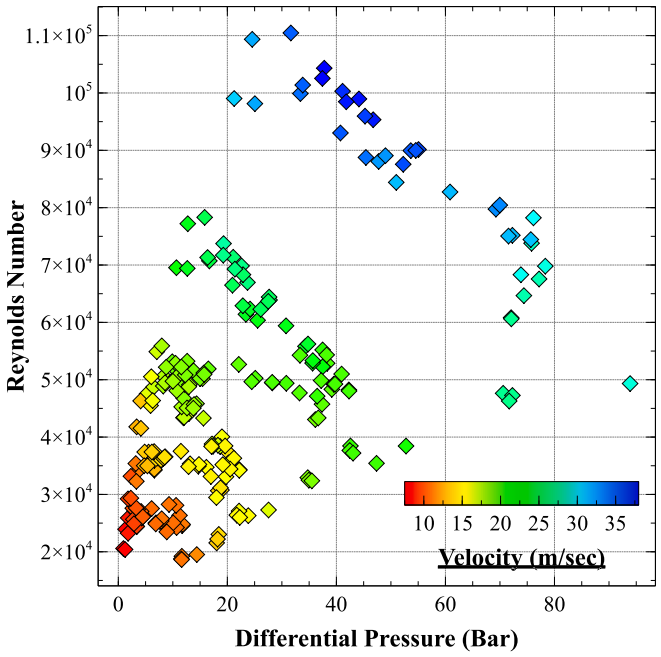

Fig. 15. Reynolds number as a function of the differential pressure. The data points are colored by the mean velocity.

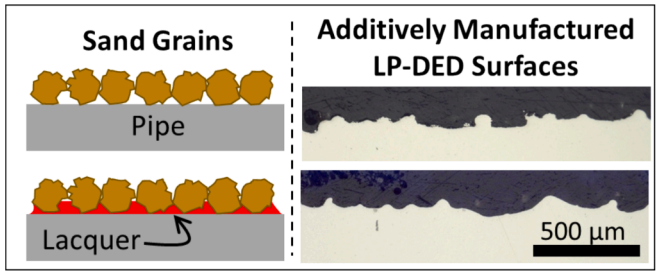

Fig. 16. Left: schematic representation of sand grains attached to the pipe surface with and without glueing lacquer as in the experiments of Darcy and Nikuradse [6,7]. Microscopic image of the surface texture resulting from LP-DED manufacturing, showing both roughness and waviness.

channel samples is 1.6 %, with a median CV of 1.1 %.

To determine the appropriate conversion from the measured surface texture to sand grain roughness, an equation is solved iteratively for the sand grain roughness factor (K_F) as shown in Equation (18). This method uses the f_D from Equation (17), which is based on the measured pressure drop, as a known variable.

$$f_D \approx f_{M1} = 1.14 + 2log_{10}\left(\frac{D_{h2}}{S_T \bullet K_F}\right)^{-2} \quad (18)$$

where S_T is the measured surface texture/roughness (i.e., Ra, Pp, Sa, Sk), and K_F is the sand grain roughness factor. An iterative optimization was run for each data set that modified the K_F until the difference between f_{M1}, the new friction factor, and f_D was within 0.1 %. The $S_T \bullet K_F$ value is then equal to K_s.

To incorporate K_s into friction factor correlations, Stimpson suggested using a parameter to normalize the value of the sand grain roughness with the hydraulic diameter (Ks/Dh) which allows for a comparison to the mean directional roughness (Ra/Dh) [57]. However, Stimpson only considered L-PBF as-built channels with rough texture variations, which did not include any partially or fully polished channel data. Wildgoose used a similar method to normalize additional data sets using Ks/Dh, but again with as-built L-PBF samples and no polishing

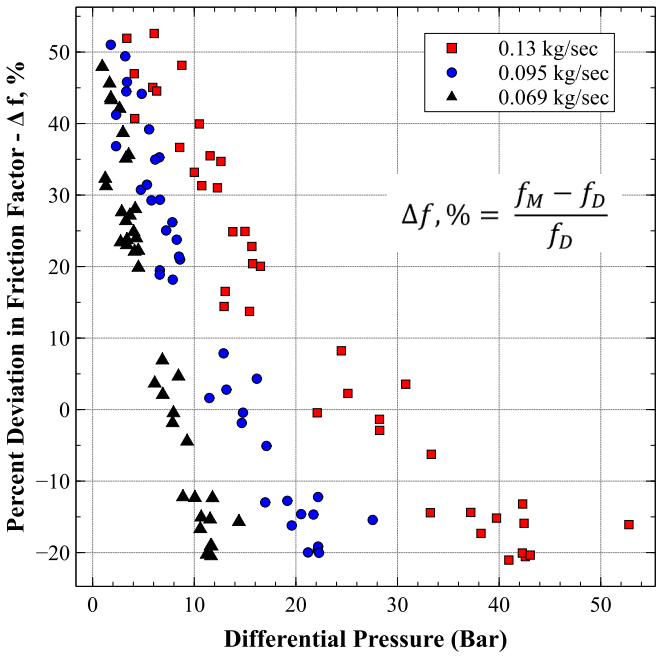

Fig. 17. Percent deviation between the experimentally determined f_D and explicit f_M plotted with differential pressure. The points indicate the fixed mass flow rates when the venturi was installed.

[39]. Wildgoose omitted Ra/D_h values below 0.007, which is the ratio of interest for this current experiment using surface enhancements. Stimpson and Wildgoose employed micro-CT scanning to obtain the roughness parameters. While micro-CT could measure features as small as 30 μm, the uncertainty estimated for Ra was 4 μm.

Fig. 18 presents the experimental data for various surface enhancement methods, showing the sand grain roughness (K_S/D_{h2}) and surface roughness/texture (S_T/D_{h2}) normalized with the hydraulic diameter. In each plot, K_S/D_{h2} remains constant, as it is directly calculated to equate f_{M1} with f_D in Equation (18). The normalized surface texture measurements (Ra/D_{h2}, Pp/D_{h2}, Sa/D_{h2}, Sk/D_{h2}) vary, filtering different surface features like roughness, waviness, and extreme peaks and valleys. Optimization based on mean filtered roughness (Ra) shows the least error with a linear fit. The primary profile (Pp), a directional measurement including full texture, shows some linearity, but the slope plateaus at Pp/D_{h2} of 0.05. The average areal texture (Sa) and core texture depth (Sk) exhibit some linearity but with greater scatter.

The correct prediction of the friction factor is essential for the design of heat exchanger channels; therefore the value of K_S must be determined, which in turn requires the value of K_F. Fig. 19 displays a plot of the values of K_F as a function of the measured surface texture/roughness parameters. Regardless of the surface texture/roughness parameter, the absolute K_S value can be computed with the value of f_D. Based on the various surface texture/roughness parameters the range of K_S is 4.8 to 167 ± 0.26 μm, corresponding to the enhanced samples and as-built, respectively. Ra and Sa, defined as average values, fail to capture the peak-to-valley range of the entire surface profile, leading to a broader range for K_F. Averaging all Ra values, as shown in Fig. 19, yields a K_F value of 4.8. In comparison, the range suggested in section 3.4 is 5.863 to 7. Other researchers suggested a K_F of 0.2 to 0.4 for ground or machined surfaces [58], which aligns with Ra in the 3 to 5 μm range. Based on these observations and as made evident by Fig. 19, the value of K_F is directly related to the roughness/texture and it cannot be assumed as a single constant.

The value of K_F for the Pp is much lower and its average value is 0.66. This is expected since it represents all profile features including roughness and waviness and is unfiltered. As Pp approaches as a value of 110 μm, indicative of as-built surfaces, the K_F approaches a value of 1. This observation provides some evidence that Pp could be used as a first-attempt approximation of the value of K_S when the surface is left in the as-built condition. The K_F related to Sa is lower than for Ra because the measured texture across the entire surface, with higher peaks and valleys, is captured. The average value of K_F is 0.84 related to Sk and indicates a linear trend with the absolute Sk. As-built roughness channels display a plateau in both Sa and Sk, but the friction factor remains relatively unchanged, suggesting the peak roughness sublayer may have been reached.

Table 5 provides the linear equations in terms of the K_S/D_{h2} ratio for the computation of the texture parameters resulting from the fitting of the experimental data. A linear fit of the K_S/D_{h2} *to the* Ra/D_{h2} parameter indicates a coefficient of determination of 95 %. The primary profile (Pp) texture parameter revealed the highest proportional variance at 85.7 %. The coefficient of determination for the Sa texture parameter was 88.2 % and Sk at 90.1 %.

3.6. Friction factor correlation and mechanism

This section summarizes the data used to calculate the friction factor based on a new correlation (Equation (11) and Table 5) and hydraulic diameter in Equation (8). The surface profile characteristics and distinct texture types are presented in relation to their correlation with the experimental friction factor.

Using the linear fit of Ra from Table 5, a correlation for f_M was developed and results are presented in Fig. 20. The values calculated with the new correlation (reported as circles), show improved accuracy by over 20 % compared to the prior correlation (shown by triangles), which used a constant value of K_S. This new correlation also expands the applicable range of surface textures, as previous studies only considered fully rough, as-built tubes or channels. The new correlation becomes less accurate when the friction factor falls below 0.03, as surface roughness and waviness decrease. At this transition, calculating D_h (indicated by squares on Fig. 20) using the traditional definition of hydraulic diameter ($4A/P$) may be more appropriate with the new linear fit model for K_S/D_{h2}. Several datasets at $f < 0.3$, not shown in Fig. 20, produced negative values for K_S when using D_{h2}. Switching to D_h corrects these negative values, but the predicted f may still be lower than the experimental values, as shown by the shift between D_{h2} and D_h predictions.

The surface texture is the result of randomly distributed adhered powder particles contributing to roughness, as well as of melt pool undulations and of build layers causing periodic and random macro waviness [2]. Thus, the orientation of these surface features relative to the flow direction affect the value of K_S. The channels utilized in the experiments described here were fabricated by depositing layers while moving the LP-DED nozzle in the vertical direction, therefore surface roughness is caused by randomly distributed particles and directionality is inconsequential. The direction in which the waviness is measured should be based on the direction of the flow and not the direction of the build. In this experiment, with the deposition in the vertical direction the macro-waves are perpendicular to the flow direction.

To establish the mathematical relationship between the surface texture parameters and the friction factor, as well as the pressure drop, the experimental data were limited to those related to channels having a mean flow areas of 6.64 mm^2 ± 10 %. Fig. 21 presents a chart showing values of Darcy friction factor as a function of the measured maximum roughness peak height and maximum waviness height. The plot indicates that the roughness peaks, primarily due to the adhered powder particles, are the main cause of the variation of the friction factor. Adhered particles increase flow resistance by destroying the laminar sublayer within the boundary layer through the formation of eddies. However, Fig. 21 also indicates the combined effect of the roughness peak height and maximum waviness height to achieve a friction factor lower than 0.05. As the powder-induced peaks are eliminated, the valleys resulting from the waviness cause flow recirculation that results in local velocity gradients.

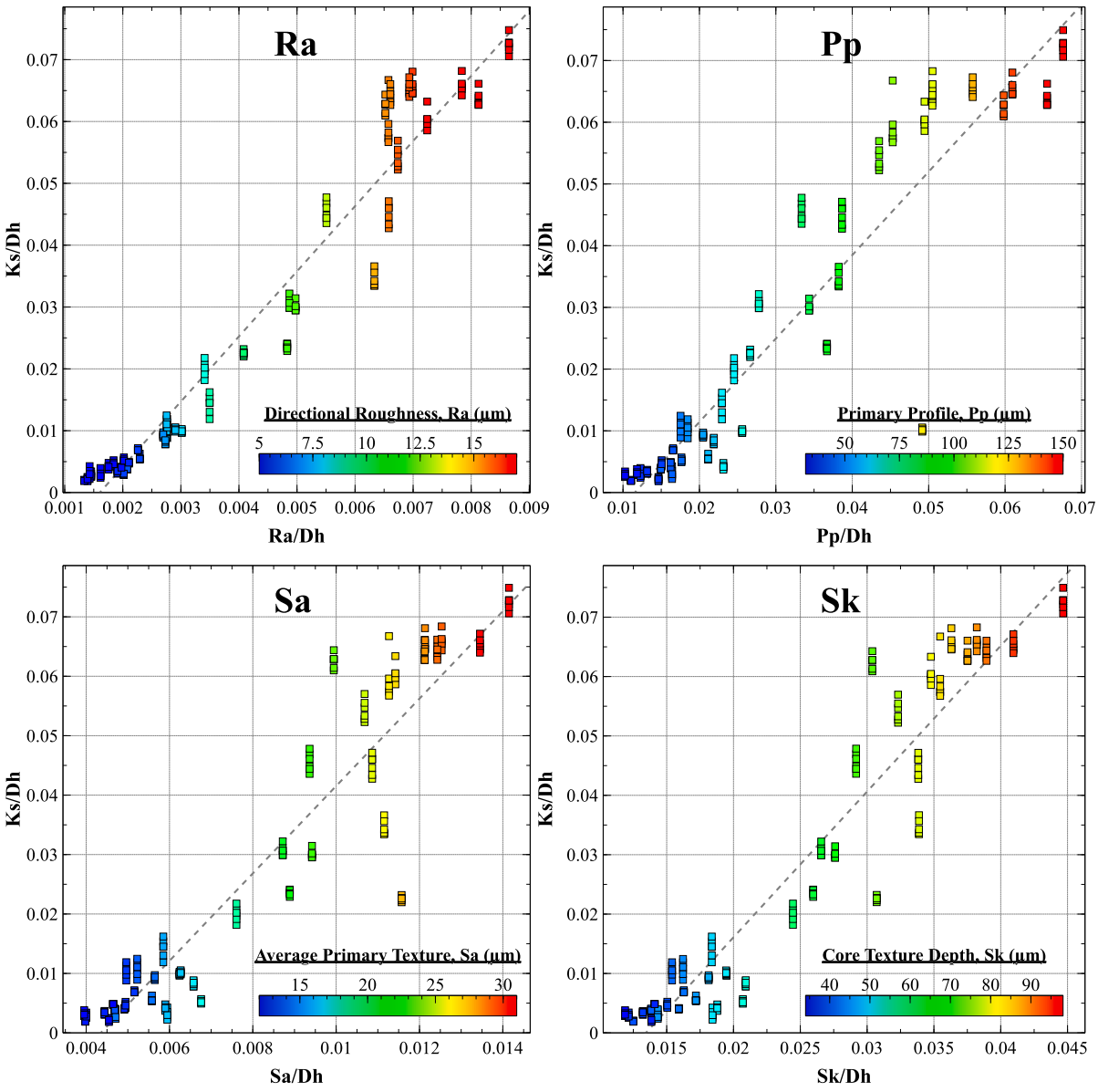

Fig. 18. Sand grain roughness (K_S /D_{h2}) as a function of the surface roughness/texture parameters (S_T /D_{h2}) normalized by hydraulic diameter. The points are colored according to the measured roughness or texture values indicated for Ra, Pp, Sa, and Sk.

To assess the contributions of the valleys, a 3D functional texture parameter called void volume was evaluated for all channels. The void volume represents the space contained within surface texture that can trap fluid, defined as the volume between all peaks and valleys relative to an idealized flat plane fitted at the highest points of the surface. This plane can then be offset in the Z-orientation (moving −Z towards the bottom of surface) to evaluate the peaks, core texture, and valleys. The void volume is normalized based on the volume per unit area, with units $\mu m^3/\mu m^2$.

Fig. 22 displays the comparison of the roughness maximum profile peak height (Rp) with the dale void volume (Vvv). The Vvv of the as-built samples have a range of 2.7 to 4.6 μ $m^3/\mu m^2$ due to heightened peaks and extreme valleys, often caused by adjacent particles; this is 61 % of the total range shown on the plot. As surface enhancements reduce the roughness peaks and corresponding void volume, flow constriction and surface friction also decrease. The data suggest that an ideal void volume below ~ 2.3 $\mu m^3/\mu m^2$ is necessary to achieve a friction factor under 0.04. To approach a friction factor of 0.03, both peak removal nearing planarization and valley reduction are essential.

To reduce the friction factor, several surface texture attributes must be properly controlled during the channel processing, as indicated by the observed data. Fig. 23 shows the comparison of the primary profile peak height (Pp) with the f_D. The primary profile incorporates both roughness and waviness surface attributes that affect the friction factor based on both roughness height and length scales. One of the values (CMP-B8) was identified as an outlier due to an erroneous Pp measurement and is not shown. The variation in the surface profile correlates to four distinct texture types and their corresponding reduction in the experimental friction factor: 1) roughness peaks, 2) peak smoothing/reduction, 3) minimized roughness and combined waviness and 4) valley reduction. These regions were selected arbitrarily based on the data set groupings observed in Fig. 23 and their corresponding f_D.

The region labeled '*Roughness peaks*' is characterized by adhered powder particles that cause the highest friction factor. These peaks must be completely removed to reduce the friction factor. They significantly disrupt the roughness sublayer, increasing drag due to turbulent eddy structures [59], and causing flow recirculation in deep valleys. As a result, the flow area becomes constricted, with f_D exceeding 0.07, likely

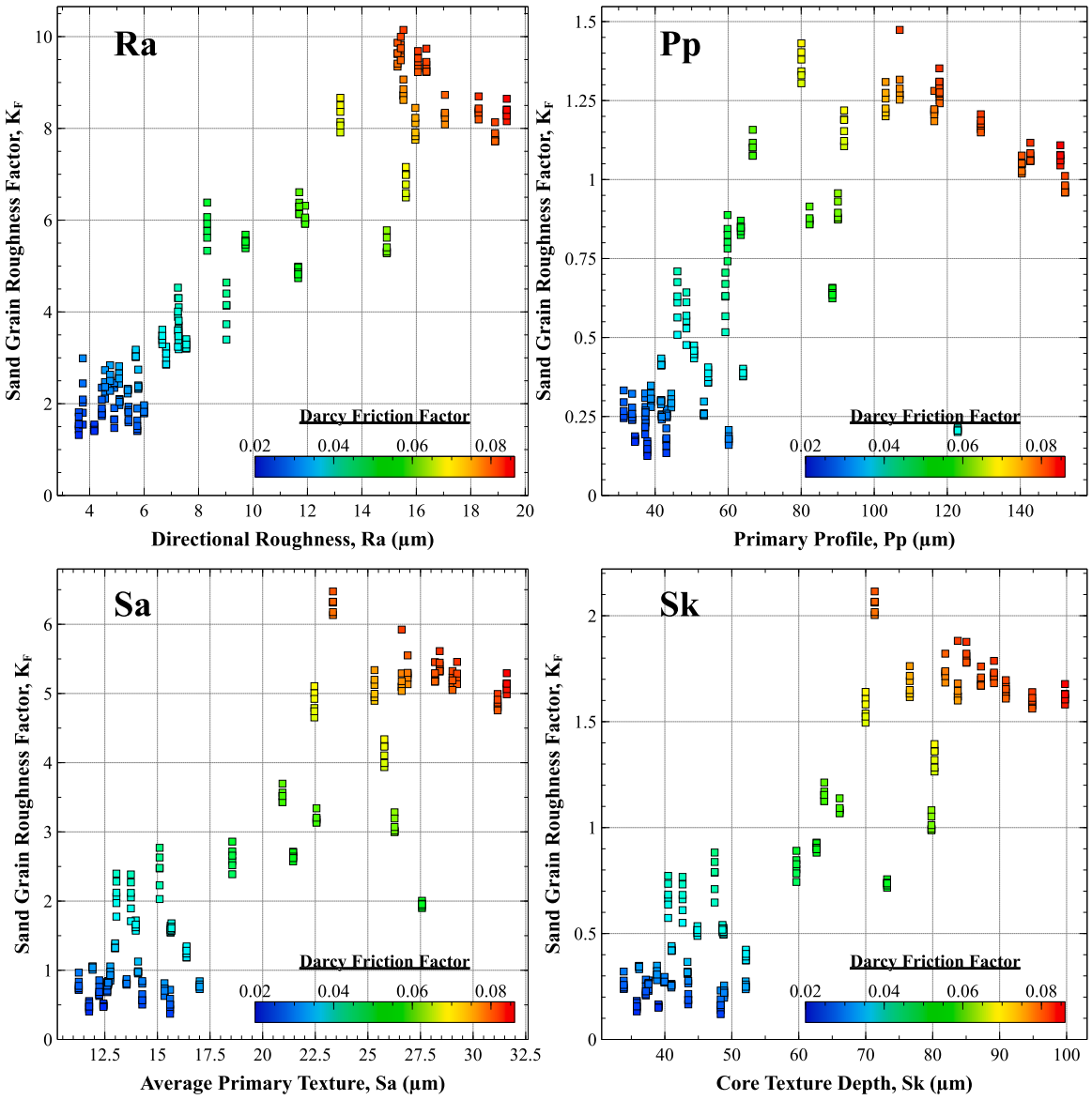

Fig. 19. Values of sand grain roughness factor based on Equation (18) as a function of the measured surface texture/roughness values. The data sets are colored according to the value of f_D.

Table 5
Summary of the linear fit of K_S/D_{h2} for texture parameters Ra, Pp, Sa, and Sk based on the data sets from Fig. 18.

Texture Parameter	Linear Fit for K_S/D_{h2}
Ra	$\frac{K_S}{D_{h2}} = 10.535\frac{Ra}{D_{h2}} - 0.0169$
Pp	$\frac{K_S}{D_{h2}} = 1.3517\frac{Pp}{D_{h2}} - 0.0156$
Sa	$\frac{K_S}{D_{h2}} = 7.3534\frac{Sa}{D_{h2}} - 0.032$
Sk	$\frac{K_S}{D_{h2}} = 2.4545\frac{Sk}{D_{h2}} - 0.033$

due to the roughness sublayer extending into the outer layer. Perry et al. suggest that eddies can match the roughness height, extending into the core flow and further restricting the flow area [56]. The as-built channels and many AFM processed channels include roughness peak features. The Pp must be reduced by 36 % by eliminating the powder induced roughness peaks before peak smoothing is present and the friction factor is reduced by 25 %. The region labeled 'Peak Smoothing/Reduction' on Fig. 23 indicates partially removed, rounded, and sometimes smeared peaks on the surface, resulting in an f_D of 0.06 ± 0.01. SEM images in section 3.1 reveal remnants of adhered powder particles on the surface of the AFM-processed channels. The surface exhibits smeared or reduced peaks, where partial particles blend into the subsurface. These features correspond to a *'peak smoothing and reduction'* (as indicated in Fig. 23), but residual particles are still present.

To further reduce surface friction, roughness peaks must be fully eliminated and macro waviness reduced, as indicated in the *'Minimized Roughness/Combined Waviness'* region in Fig. 23. Achieving surface planarization requires the complete elimination of all powder particles resulting in a reduction of the peak profile by 30 % to obtain a friction factor below 0.05. The depth of the roughness and waviness peaks and resulting flow micro-eddies, can exacerbate the flow constriction. These eddies are influenced by the height and spacing of the roughness and waviness peaks. This aligns with Coleman's research on discrete geometric ribs causing variations in flow disturbances based on the distance between ribs [60]. Therefore, the complete removal of powder particles and the reduction of the spatial waviness peaks are crucial.

Minimizing the surface peaks and reducing macro waviness leaves

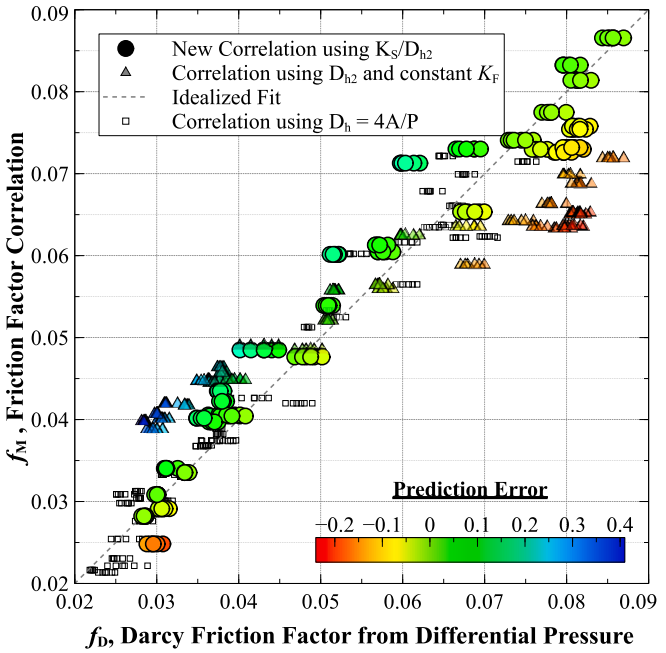

Fig. 20. Correlation of f_M using the K_S /D_{h2} and Ra/D_{h2} linear fit method in relation to the f_D . The points are colored according to the prediction error from the idealized fit.

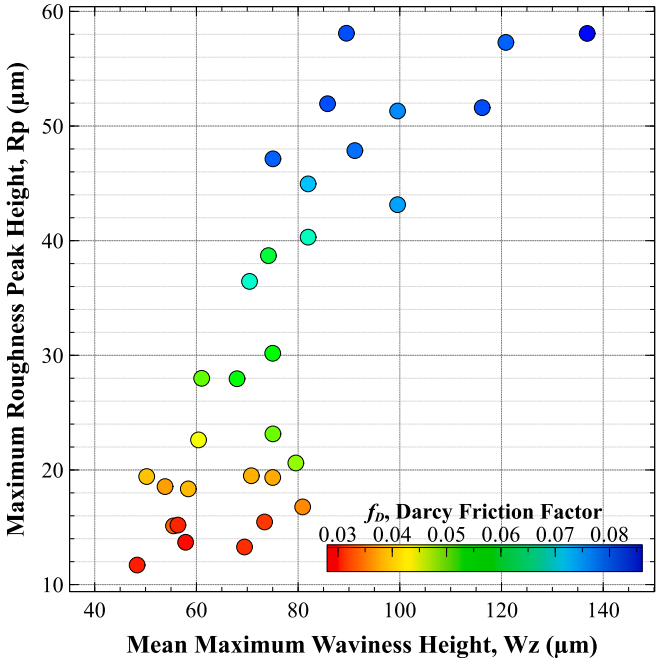

Fig. 21. Maximum Peak Height (Rp) compared with maximum waviness height (Wz) for channel areas = 6.64 mm^2 ± 10 %, ṁ = 0.13 kg/sec. The data sets are colored according to the f_D .

minor valleys present on the surface. At this surface condition, the minor peaks and associated valleys likely become submerged in the sublayer flow, exerting minimal influence on skin friction [58]. The primary profile shows an average reduction of 27 % when transitioning from the 'minimized roughness/waviness' to the 'valley reduction' region. Fig. 23 shows the primary profile reduction as an exponential curve, correlating with the friction factor reduction, where minimal material removal from waviness causes only slight changes in the friction factor.

Modifying the surface through material removal is essential to

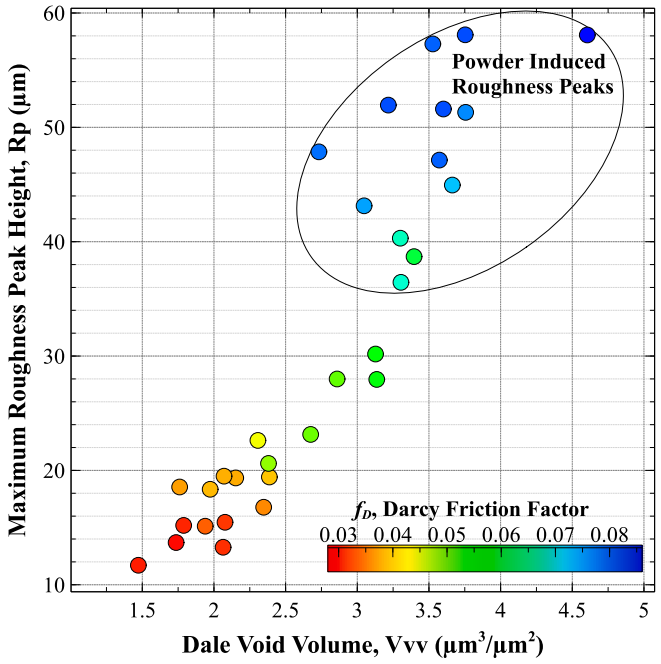

Fig. 22. Maximum peak height (Rp) compared to the dale void volume (Vvv) indicating the remaining valleys; channel areas = 6.64 mm^2 ± 10 %, ṁ = 0.13 kg/sec. The data sets are colored according to the f_D .

achieve a planar surface to minimize flow friction. Heat exchangers are designed to meet performance targets based on mass flow rate, pressure drop, and heat transfer coefficient. This research focuses on specifying an as-built geometry, where surface alterations ensure the intended geometry and flow conditions are met. To achieve this, the required material removal must align with the heat exchanger's technical specifications and surface conditions (as shown in Fig. 23). Technical merit should also include processing economics; excessive material removal leads to wasted powder feedstock, longer LP-DED build times, and extended post-processing, while insufficient removal results in high differential pressure, potentially missing performance targets.

Fig. 24 illustrates the value of material removal per side as a function of the Dale void volume measurement. The CM process exhibits the highest material removal (over 90 µm), leading to the largest cross-sectional area but failing to achieve the lowest f_D. While CM is effective at removing powder particles and reducing partial waviness peaks, it does not fully planarize the surface by removing valleys. In contrast, CMP effectively reduces waviness peaks through abrasive media polishing, which also minimizes valleys, as shown by the reduction in Vvv (Fig. 24). Removing 60 µm of material per side, combined with planarization, results in a friction factor of 0.03. Targeting material removal of 84 µm (a 40 % increase) reduces the f_D by an additional 7 %, bringing it down to 0.028.

The AFM process reduces surface friction with minimal material removal (less than 25 µm), but results in a f_D exceeding 0.05. Further reduction of the friction factor may be possible with increased slurry pressure, flow rate, resulting in more aggressive abrasive milling. While CM minimizes tooling and overall costs compared to AFM and CMP, all processes can be used to modify surfaces and adjust the friction factor based on end-use requirements. Future work may explore a combination of techniques to minimize material removal while effectively reducing surface roughness and waviness.

4. Conclusions

The effects of three surface enhancement methods—abrasive flow machining, chemical milling, and chemical mechanical polishing— on

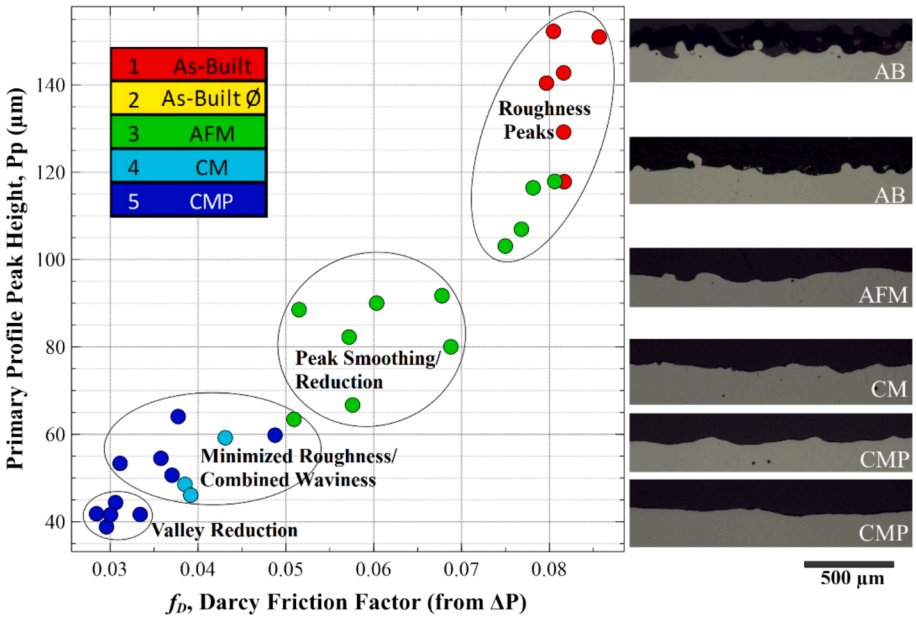

Fig. 23. Surface attributes affecting reduction of the friction factor. The color of the symbols is associated to the surface enhancement process as listed in the legend. Right: The cross-section microscopic images are representative of the surfaces for each of the enhancement processes.

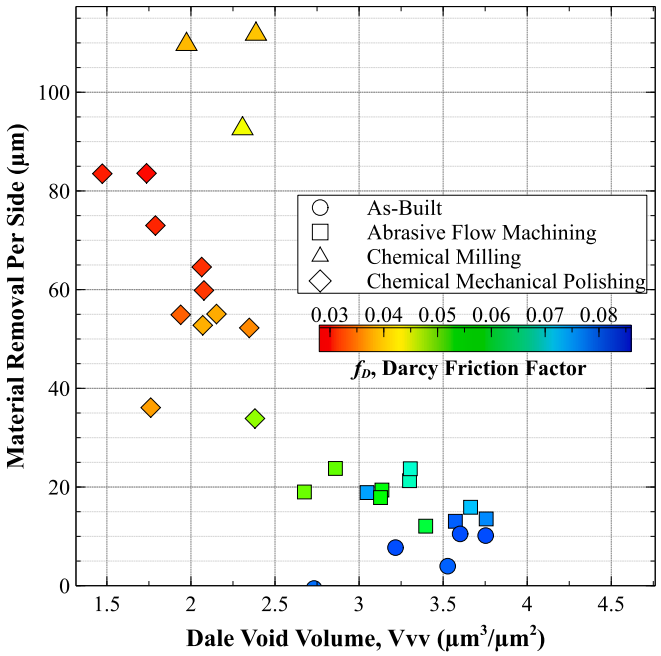

Fig. 24. Material removal per side and dale void volume compared to the Darcy friction factor. The symbol markers indicate the surface enhancement process and data sets are colored according to the f_D .

the fluid dynamic performance of heat exchanger additively manufactured laser powder directed energy deposition (LP-DED) microchannels were compared through flow testing. As-built channels were used to determine the performance benchmark. All the built and tested channels feature square a cross section measuring 2.54 x 2.54 mm. The channels were fabricated from the NASA HR-1 (Fe-Ni-Cr) alloy because one target application is the cooling system of rocket nozzles, however results are applicable to heat exchangers realized with the LP-DED process in general.

Flow testing was conducted at various mass flow rates to characterize the pressure drop for each channel. Following experimental testing, the sample channels underwent destructive evaluation, whereby inner surfaces were characterized using scanning electron microscopy (SEM), optical microscopy, and optical surface texture analysis. Based on this detailed study and using the detailed data obtained during material characterization, a friction factor correlation was developed. The correlation includes texture–dependent parameters which in turn relate to equivalent sand grain roughness. The sand grain roughness, originally based on the experiments of Darcy and Nikuradse, is commonly used for friction factor correlations. However, surfaces produced by the LP-DED process are more complex and cannot be characterized with sand grains values.

The following conclusions can be drawn:

- Surface enhancements significantly reduced boundary layer turbulence by eliminating adhered powder and planarizing the surface, resulting in a tenfold reduction in pressure drop.
- The surface enhancement techniques [abrasive flow machining (AFM), chemical milling (CM), and chemical mechanical polishing (CMP)] produce distinct surface attributes (peaks and valleys associated with roughness and waviness) due to differences in the way material is removed, thus surface flow drag is different.
- The surface texture was varied across the channels using enhancements applied to the as-built surfaces. The filtered Ra ranged from 3.6 to 19.3 µm, primary Sa ranged from 11.3 to 31.6 µm, primary Sk ranging from 33.9 to 99.8 µm, and Pp from 31.4 to 152.3 µm.
- A new definition of hydraulic diameter, dependent on the value of the characterized cross–sectional area and core surface texture (Sk), has been proposed and validated with experimental data. This definition reduces the error associated with conventional definitions of hydraulic diameter, which depend solely on cross-sectional area and perimeter. This new expression of the hydraulic diameter allows to overcome the large error due to the strong biases occurring in the case of highly textured surfaces. For example, the value of the actual perimeter of the cross-section of as-built channels is widely different from its design value, which assumes a perfect geometry, free from any irregularity.
- None of the friction factor correlations documented in the literature provide values that match those computed with the Darcy friction factor obtained from measured differential pressures, including the Colebrook-White correlation. A new friction factor correlation for

AM channels was obtained by modifying the sand grain roughness expression and that of the hydraulic diameter so as to take into account microscopic surface features. The predictive capabilities of the new correlation has been validated.

- The variation in the surface profile correlates to four distinct types of texture and relates to the reduction in the experimental friction factor: 1) roughness peaks, 2) peak smoothing/reduction, 3) minimized roughness and combined waviness and 4) valley reduction.
- A method was developed to predict sand grain roughness based on variations in the surface texture and associated areal and directionally measured values.
- The proposed method for characterizing equivalent sand grain roughness calculates friction factor values with less than 20 % deviation from the experimental data, whereas values calculated using other correlations in the literature deviate by approximately 50 %.
- The primary profile, which considers surface roughness and waviness, provides a reasonable first-order approximation of equivalent sand grain roughness for as-built surfaces.
- The average directional roughness normalized by hydraulic diameter (*Ra/Dh*) provides the best fit for determining the equivalent sand grain roughness from experimental data.

Optimal material removal is essential to eliminate roughness peaks and planarize waviness. Abrasive methods effectively achieve planarization, whereas chemical milling does not allow for waviness to be completely eliminated. A minimum removal thickness of 60 μm per side is necessary to achieve a friction factor below 0.03. Removing 84 μm of material (40 % more than the minimum) resulted in a further 7 % reduction in friction factor. Surface enhancements applied to microchannels produced by the LP-DED process demonstrated that surfaces can be modified to meet specific requirements. This data enables designers to tailor surfaces for fluid friction factors, fatigue life, corrosion resistance, heat transfer, and aesthetics.

Funding and Acknowledgements

This research was funded by NASA under additive manufacturing development efforts through the Optimized and Repeatable Components using Additive (ORCA) and SLS Liquid Engines Office (LEO) project. This paper describes objective technical results and analysis. Any subjective views or opinions that might be expressed in the paper do not necessarily represent the views of the National Aeronautics and Space Administration (NASA) or the United States Government. Thank you to industry partners RPM Innovations (RPMI), Extrude Hone, REM Surface Engineering, and TechMet. The authors also acknowledge the use of Veusz, Winplot, and ImageJ software.

CRediT authorship contribution statement

Paul Gradl: Resources, Project administration, Methodology, Investigation, Funding acquisition, Formal analysis, Data curation, Conceptualization. **Angelo Cervone:** Writing – review & editing, Supervision, Project administration. **Piero Colonna:** Writing – review & editing, Supervision, Project administration.

Declaration of competing interest

The authors declare that they have no known competing financial interests or personal relationships that could have appeared to influence the work reported in this paper.

Appendix A. Supplementary data

Supplementary data to this article can be found online at https://doi.org/10.1016/j.matdes.2025.113673.

Data availability

Data will be made available on request.

References

[1] P. Gradl, A. Cervone, P. Colonna, Integral Channel Nozzles and Heat Exchangers using Additive Manufacturing Directed Energy Deposition NASA HR-1 Alloy, in: 73rd Int. Astronaut. Congr., Paris, France, 2022: p. IAC-22,C4,2,x73690.
[2] P. Gradl, A. Cervone, P. Colonna, Influence of build angles on thin-wall geometry and surface texture in laser powder directed energy deposition, Mater. Des. 234 (2023) 112352, https://doi.org/10.1016/j.matdes.2023.112352.
[3] P.R. Gradl, A. Cervone, E. Gill, Surface texture characterization for thin-wall NASA HR-1 Fe – Ni – Cr alloy using laser powder directed energy deposition (LP-DED),, Adv. Ind. Manuf. Eng. 4 (2022) 100084, https://doi.org/10.1016/j.aime.2022.100084.
[4] P. Gradl, A. Cervone, P. Colonna, Development and experimental evaluation of surface enhancement methods for laser powder directed energy deposition microchannels for laser powder directed energy deposition microchannels, Virtual Phys. Prototyp. 19 (2024) e2345389, https://doi.org/10.1080/17452759.2024.2345389.
[5] L.F. Moody, Friction Factors for Pipe Flow, J. Fluids Eng. Trans. ASME 66 (1944) 671–678, https://doi.org/10.1115/1.4018140.
[6] H. Darcy, Recherches Experimentales Relatives Au Mouvement De L'Eau Dans Les Tuyaux, Mallet- Bachelier- Bachelier, Paris, 1857.
[7] J. Nikuradse, Laws of flow in rough pipes [Stromungsgesetze in Rauen Rohren], VDI-Forschungsheft, Beilage Zu Forsch. Auf Dem Gebiete Des Ingenieurwesens, Ausgabe B Band 4 English Transl. NACA Tech. Memo 1292, 1950. 361 (1933) 315.
[8] C.F. Colebrook, Experiments with fluid friction in roughened pipes, Proc. Roy. Soc. Ser. Math. Phys. Sci. 161 (1937) 367–381.
[9] C.F. Colebrook, Turbulent flow in pipes with particular reference to the transition region between the smooth and rough pipe laws, J. Inst. Civil. Eng. Lond. 11 (1939) 133–156.
[10] J.B. Taylor, A.L. Carrano, S.G. Kandlikar, Characterization of the effect of surface roughness and texture on fluid flow - Past, present, and future, Proc. 3rd Int. Conf. Microchannels Minichannels, 2005 PART A (2005) 11–18. https://doi.org/10.1016/j.ijthermalsci.2006.01.004.
[11] S. Kandlikar, S. Garamella, Mi. King, Heat Transfer and Fluid Flow in Minichannels and Microchannels, 2nd ed., Elsevier, 2014. https://doi.org/10.1016/c2011-0-07521-x.
[12] T. Santese, A. Söndgerath, S. Soller, B. Latini, C. Manfletti, Experimental and Numerical Investigation of Frictional Behavior and Heat Transfer in 3D Printed Rocket Engine Cooling Channels, in: Sp. Propuls. Conf. 2024, Glasgow, 2024: p. 216.
[13] S.T. Mcclain, J.C. Snyder, D.R. Hanson, R.F. Kunz, K.A. Thole, Flow in a Simulated Turbine Blade Cooling Channel with Spatially Varying Roughness Caused by Additive Manufacturing Orientation, in, ASME Turbo Expo 2020 (2020) 1–14.
[14] N. Richermoz, D. Gloriod, T. Baffie, Z. Anxionnaz-Minvielle, P. Coste, Roughness Effect on Thermal-Hydraulic Performances of Additively Manufactured Meandering Mini-Channels, Heat Transf. Eng. (2023) 1–17, https://doi.org/10.1080/01457632.2023.2275234.
[15] L. Zhou, Y. Zhu, H. Liu, T. He, C. Zhang, H. Yang, A comprehensive model to predict friction factors of fluid channels fabricated using laser powder bed fusion additive manufacturing, Addit. Manuf. 47 (2021) 102212, https://doi.org/10.1016/j.addma.2021.102212.
[16] J.C. Snyder, K.A. Thole, Effect of additive manufacturing process parameters on turbine cooling, J. Turbomach. 142 (2020), https://doi.org/10.1115/1.4046459/1074872.
[17] K.L. Kirsch, J.C. Snyder, C.K. Stimpson, K.A. Thole, D. Mongillo, Repeatability in performance of micro cooling geometries manufactured with laser powder bed fusion, 53rd AIAA/SAE/ASEE Jt, Propuls. Conf. 2017 (2017) 1–14, https://doi.org/10.2514/6.2017-4706.
[18] C.R. Hartsfield, T.E. Shelton, G.R. Cobb, R.A. Kemnitz, J. Weber, Understanding Flow Characteristics in Metal Additive Manufacturing, J. Aerosp. Eng. 34 (2021) 1–9, https://doi.org/10.1061/(asce)as.1943-5525.0001325.
[19] Y. Zhu, L. Zhou, S. Wang, C. Zhang, C. Zhao, L. Zhang, H. Yang, On friction factor of fluid channels fabricated using selective laser melting, Virtual Phys. Prototyp. 15 (2020) 496–509, https://doi.org/10.1080/17452759.2020.1823093.
[20] M. Jamshidinia, R. Kovacevic, The influence of heat accumulation on the surface roughness in powder-bed additive manufacturing, Surf. Topogr. Metrol. Prop. 3 (2015) 14003, https://doi.org/10.1088/2051-672X/3/1/014003.
[21] G. Favero, G. Berti, M. Bonesso, D. Morrone, S. Oriolo, P. Rebesan, R. Dima, P. Gregori, A. Pepato, A. Scanavini, S. Mancin, Experimental and numerical analyses of fluid flow inside additively manufactured and smoothed cooling channels, Int. Commun. Heat Mass Transf. 135 (2022) 106128, https://doi.org/10.1016/j.icheatmasstransfer.2022.106128.
[22] K. Vijetha, D. Lingaraju, G. Satish, V.S. Reddy, M.P.K. Reddy, Fabrication of microchannel heat sink using additive manufacturing technology : A review, (2024). https://doi.org/10.1177/09544089241290631.
[23] I. Kaur, P. Singh, State-of-the-art in heat exchanger additive manufacturing, Int. J. Heat Mass Transf. 178 (2021) 121600, https://doi.org/10.1016/j.ijheatmasstransfer.2021.121600.

[24] E. Maleki, S. Bagherifard, M. Bandini, M. Guagliano, Surface post-treatments for metal additive manufacturing: Progress, challenges, and opportunities, Addit. Manuf. 37 (2021) 101619, https://doi.org/10.1016/j.addma.2020.101619.
[25] W. Demisse, J. Xu, L. Rice, P. Tyagi, Review of internal and external surface finishing technologies for additively manufactured metallic alloys components and new frontiers, Prog. Addit. Manuf. (2023), https://doi.org/10.1007/s40964-023-00412-z.
[26] A.W. Hashmi, H.S. Mali, A. Meena, A comprehensive review on surface quality improvement methods for additively manufactured parts, 2023. https://doi.org/10.1108/RPJ-06-2021-0133.
[27] K.L. Tan, S.-H.-H. Yeo, C.H. Ong, Nontraditional finishing processes for internal surfaces and passages: A review, Proc. Inst. Mech. Eng. Part B J. Eng. Manuf. 231 (2016) 2302–2316, https://doi.org/10.1177/0954405415626087.
[28] A. Diaz, Surface texture characterization and optimization of metal additive manufacturing-produced components for aerospace applications, Addit. Manuf. Aerosp. Ind. (2019) 341–374, https://doi.org/10.1016/B978-0-12-814062-8.00018-2.
[29] P. Tyagi, T. Goulet, C. Riso, R. Stephenson, N. Chuenprateep, J. Schlitzer, C. Benton, F. Garcia-Moreno, Reducing the roughness of internal surface of an additive manufacturing produced 316 steel component by chempolishing and electropolishing, Addit. Manuf. 25 (2019) 32–38, https://doi.org/10.1016/j.addma.2018.11.001.
[30] M. Kulkarni, F. Gao, H. Liang, Chemical-mechanical polishing (CMP): a controlled tribocorrosion process, Tribocorrosion Passiv. Met, Coatings (2011) 498–518e, https://doi.org/10.1533/9780857093738.3.498.
[31] E. Lemmon, Thermophysical Properties of Fluids, National Institute of Standards and Technology (NIST), Gaithersburg, Maryland, 2009.
[32] A. Thompson, N. Senin, C. Giusca, R. Leach, Topography of selectively laser melted surfaces: A comparison of different measurement methods, CIRP Ann. - Manuf. Technol. 66 (2017) 543–546, https://doi.org/10.1016/j.cirp.2017.04.075.
[33] A. Mirabal, I. Loza-hernandez, C. Clark, D.E. Hooks, M. Mcbride, J.A. Stull, Roughness measurements across topographically varied additively manufactured metal surfaces, Addit. Manuf. 69 (2023) 103540, https://doi.org/10.1016/j.addma.2023.103540.
[34] C.A. Schneider, W.S. Rasband, K.W. Eliceiri, NIH Image to ImageJ: 25 years of image analysis, Nat. Methods 9 (2012) 671–675, https://doi.org/10.1038/nmeth.2089.
[35] A.J. Brooks, A. Dhakad, A. Diaz, D. Kowalik, Toward Understanding the Role of Surface Texture for Additively Manufactured Metal Parts, Struct. Integr. Addit. Manuf. Mater. Parts ASTM Inter (2020) 61–87, https://doi.org/10.1520/stp163120190160.
[36] P. Pawlus, R. Reizer, M. Wieczorowski, Functional importance of surface texture parameters, Materials (basel). 14 (2021) 1–29, https://doi.org/10.3390/ma14185326.
[37] D. Brkić, Review of explicit approximations to the Colebrook relation for flow friction, J. Pet. Sci. Eng. 77 (2011) 34–48, https://doi.org/10.1016/j.petrol.2011.02.006.
[38] Y.A. Cengel, J.M. Cimbala, Fluid Mechanics: Fundamentals and Applications, 3rd ed., McGraw-Hill, New York, N.Y., 2014.
[39] A.J. Wildgoose, K.A. Thole, E. Tuneskog, L. Wang, Roughness Related to Cooling Performance of Channels made through Additive Manufacturing, in: Proc. ASME Turbo Expo 2023, ASME Turbomachinery Technical Conference and Exposition, Boston, Massachusetts, 2023.
[40] K. Rehme, K. Nuclear, Simple Method of Predicting Friction Factors of Turbulent Flow in Non-Circular Channels, Int. J. Heat Mass Transf. 16 (1973) 933–950.
[41] G. Demeneghi, P. Gradl, J.R. Mayeur, K. Hazeli, Size Effect Characteristics and Influences on Fatigue Behavior of Laser Powder Bed Fusion of GRCop-42 Copper Alloy, Heliyon 10 (2023) e28679, https://doi.org/10.1016/j.heliyon.2024.e28679.
[42] D. June, J.R. Mayeur, P. Gradl, A. Wessman, K. Hazeli, Effects of Size, Geometry, and Temperature on Additively Manufactured Ti-6Al-4V Titanium Alloy 1 2, Addit. Manuf. 80 (2024) 103970, https://doi.org/10.1016/j.addma.2024.103970.
[43] S.G. Kandlikar, D. Schmitt, A.L. Carrano, J.B. Taylor, Characterization of surface roughness effects on pressure drop in single-phase flow in minichannels, Phys. Fluids 17 (2005) 100606, https://doi.org/10.1063/1.1896985.
[44] M. Kadivar, D. Tormey, G. Mcgranaghan, A review on turbulent flow over rough surfaces: fundamentals and theories, Int. J. Thermofluids (2021) 100077, https://doi.org/10.1016/j.ijft.2021.100077.
[45] P.K. Swamee, A.K. Jain, Explicit Equations for Pipe-Flow Problems, J. Hydraul. Div. 102 (1976) 657–664, https://doi.org/10.1061/JYCEAJ.0004542.
[46] V. Mileikovskyi, T. Tkachenko, Precise Explicit Approximations of the Colebrook-White Equation for Engineering Systems, Lect. Notes Civ. Eng. 100 LNCE (2021) 303–310. https://doi.org/10.1007/978-3-030-57340-9_37.
[47] Ž. Ćojbašić, D. Brkić, Very accurate explicit approximations for calculation of the Colebrook friction factor, Int. J. Mech. Sci. 67 (2013) 10–13, https://doi.org/10.1016/J.IJMECSCI.2012.11.017.
[48] A. Avci, I. Karagoz, A novel explicit equation for friction factor in smooth and rough pipes, J. Fluids Eng. Trans. ASME 131 (2009) 0612031–0612034, https://doi.org/10.1115/1.3129132/444690.
[49] G. Plascencia, L. Díaz-Damacillo, M. Robles-Agudo, On the estimation of the friction factor: a review of recent approaches, SN Appl. Sci. 2 (2020) 1–13, https://doi.org/10.1007/s42452-020-1938-6.
[50] M. Jaric, S. Genić, I. Arandjelović, P. Kolendić, M. Jarić, N. Budimir, V. Genić, A Review of Explicit Approximations of Colebrook's Equation, FME Trans. (2011) 39–67.
[51] T. Adams, C. Grant, H. Watson, A Simple Algorithm to Relate Measured Surface Roughness to Equivalent Sand-grain Roughness, Int. J. Mech. Eng. Mechatronics 1 (2012) 66–71. https://ijmem.avestia.com/2012/008.html.
[52] V.T. Forster, Performance Loss of Modern Steam-Turbine Plant due to Surface Roughness, Proc. Inst. Mech. Eng. 181 (1966) 404–405, https://doi.org/10.1243/PIME_PROC_1966_181_038_02.
[53] C.C. Koch, L.H. Smith, Loss Sources and Magnitudes in Axial-Flow Compressors, Am. Soc. Mech. Eng. (1975) 411–424.
[54] M.N. Goodhand, K. Walton, L. Blunt, H.W. Lung, R.J. Miller, R. Marsden, The Limitations of using "ra" to describe surface roughness, J. Turbomach. 138 (2016), https://doi.org/10.1115/1.4032280.
[55] M.R. Raupach, R.A. Antonia, S. Rajagopalan, Rough-Wall Turbulent Boundary Layers, Appl. Mech. Rev. 44 (1991) 1–25, https://doi.org/10.1115/1.3119492.
[56] A.E. Perry, W.H. Schofield, P.N. Joubert, Rough wall turbulent boundary layers, J. Fluid Mech. 37 (1969) 383–413, https://doi.org/10.1017/S0022112069000619.
[57] C.K. Stimpson, J.C. Snyder, K.A. Thole, D. Mongillo, Scaling Roughness Effects on Pressure Loss and Heat Transfer of Additively Manufactured Channels, J. Turbomach. 139 (2016) 1–10, https://doi.org/10.1115/1.4034555.
[58] K. Bammert, H. Sandstede, Influences of Manufacturing Tolerances and Surface Roughness of Blades on the Performance of Turbines, Am. Soc. Mech. Eng. (1975) 29–36.
[59] R.J. Volino, M.P. Schultz, K.A. Flack, Turbulence structure in rough- and smooth-wall boundary layers, J. Fluid Mech. 592 (2007) 263–293, https://doi.org/10.1017/S0022112007008518.
[60] S.E. Coleman, V.I. Nikora, S.R. Mclean, E. Schlicke, Spatially Averaged Turbulent Flow over Square Ribs, J. Eng. Mech. 133 (2007) 194–204, https://doi.org/10.1061/(ASCE)0733-9399(2007)133.